Department of Physics and Astronomy
Heidelberg University

Bachelor Thesis in Physics
submitted by

Nikolas Rapp

born in Emmendingen

2023

Time-resolved imaging of CH_4 fragmentation in strong laser fields

This Bachelor Thesis has been carried out by Nikolas Rapp at the
Max Planck Institute for Nuclear Physics in Heidelberg
under the supervision of
Priv.-Doz. Dr. Robert Moshammer

Abstract

Combining a femtosecond laser with a Reaction Microscope (ReMi), time-resolved fragmentation measurements of methane (CH_4) have been done in a pump-probe scheme. By reconstructing the three-dimensional momentum for different reaction products, various dissociation pathways have been observed showing distinct angular distributions. For a better understanding of these pathways, also single-pulse measurements were examined, serving as valuable references. The main focus lay on two-body Coulomb explosions of $CH_3^+ + H^+$ and $CH_2^+ + H_2^+$. For both channels two processes were observed: One time-independent Coulomb explosion and, in the pump-probe experiment, another process depending on the time delay of the second pulse in respect to the first one. The latter is due to a two-step Coulomb explosion with both pulses being involved. Thus, during the delay-time between both the molecule starts to dissociate on an intermediate potential curve. The angular dependence of those processes was compared with the single ionized dissociations. As a result, the time delayed Coulomb explosions as well as the two dissociation channels of $CH_3^0 + H^+$ and $CH_2^0 + H_2^+$ show a break-up strongly favored along the laser polarization axis. For $CH_3^+ + H^0$ and $CH_2^+ + H_2^0$ an isotropic distribution was observed. Therefore the first two dissociation channels are possible intermediate states for the time-delayed Coulomb explosion.

Zusammenfassung

Durch Kombination eines Femtosekunden-Lasers mit einem Reaktionsmikroskop (ReMi) wurden zeitaufgelöste Messungen von Fragmentationsprozessen von Methan in einem Pump-Probe-Experiment durchgeführt. Das ReMi ermöglicht eine dreidimensionale Impuls-Rekonstruktion, wodurch unterschiedliche Winkelverteilungen für verschiedene Dissoziationsprozesse beobachtet wurden. Um ein besseres Verständnis dieser Prozesse zu erlangen, wurden die Ergebnisse mit denen eines Einfachpuls-Experimentes verglichen. Ein besonderer Fokus lag dabei auf den Zweikörper-Coulomb-Explosionen in $CH_3^+ + H^+$ und $CH_2^+ + H_2^+$. Für beide Kanäle konnte ein zeitunabhängiger sowie im Pump-Probe-Experiment ein zweiter, vom zeitlichen Abstand der beiden Pulse abhängiger, Prozess festgestellt werden. Letzterer ist auf eine zweischrittige Coulomb-Explosion zurückzuführen, in die beide Pulse involviert sind. Folglich gibt es einen Zwischenzustand, in dem das Molekül bereits beginnt zu dissoziieren. Die Winkelabhängigkeit dieser Prozesse wurde mit denen der einfach ionisierten Fragmentationsprozessen verglichen. Es stellte sich heraus, dass sowohl die beiden zeitabhängigen Coulomb-Explosionen, als auch die Dissoziationen in $CH_3^0 + H^+$ und $CH_2^0 + H_2^+$ stark bevorzugt in Laserrichtung aufbrechen. Für $CH_3^+ + H^0$ und $CH_2^+ + H_2^0$ war die Impulsverteilung dagegen isotrop. Die beiden ersteren Dissoziationen kommen daher als mögliche Zwischenzustände in Frage.

Contents

1 Introduction **7**

2 Theoretical Background **9**
2.1 Photoionization 9
2.2 Dissociation of molecular ions 11
2.3 Methane molecule 13

3 Experimental setup **15**
3.1 Femtosecond pulse laser 15
3.2 Reaction Microscope 17
3.3 Momentum reconstruction 20

4 Data analysis **23**
4.1 Single pulse dissociation 26
4.2 Single pulse Coulomb explosion 29
4.3 Pump-probe Coulomb explosion 31
4.3.1 $CH_3^+ + H^+$ Coulomb explosion 32
4.3.2 $CH_2^+ + H_2^+$ Coulomb explosion 38

5 Conclusion and Outlook **41**

A Atomic units (a.u.) **44**

1 Introduction

The structure of atoms became an intensely debated question in the late 19th and early 20th century. Experiments, discovering the electron and Rutherford's famous gold foil experiment leading him to propose the existence of a nucleus [8], made clear that the "atom" (from Greek atomos for uncuttable) could not be the smallest structure matter is made of. Several models of the atom were discussed, which also became influenced by the beginning of quantum theory. The best known semi-classical approximation, the Bohr model [27] and its further development by Sommerfeld [31], were then able to explain the discrete spectral lines of hydrogen. A full quantum mechanical treatment of atoms was first possible with the development of the Schrödinger equation. For atomic and molecular systems – neglecting relativistic and quantum field theoretical aspects – the time dependent Schrödinger equation gives the full description. However, fully solving the Schrödinger equation is only possible for simplest cases; in atomic physics this means the hydrogen atom. For larger atoms and especially for molecules more or less good approximations have to be done and large numerical effort is needed. Experiments are thus needed.

Understanding the dynamics of a system requires high time resolution. For atomic motions in molecules this corresponds to timescales in the femtosecond (10×10^{-15} s) regime. Measuring on such short timescales means that interactions initiating nuclear dynamics have to be on the same or even shorter timescale. For atoms and molecules experiments have been done with different interactions such as fast electrons [37], highly charged ions [29] as well as ultrashort laser pulses [22] as used in this thesis.

The invention of femtosecond-short laser pulses and its use for studying transition states of chemical reactions established the new field of femtochemistry in the past decades [36], for which Ahmed Zewail gained a Nobel prize in 1999. A widely used method for studying molecular dynamics in the use of two femtosecond laser pulses in a pump probe experiment: The first one ("pump pulse") excites the atom to a non-equilibrium state. Later, a second "probe pulse" is used to probe the new state of the molecule. Varying the time-delay between both pulses then provides information about the dynamics risen in the molecule after the first pulse. Those can be rotational and vibrational modes as well as dissociations of the molecule. Inferences in vibrating iodine molecules were observed by Katsuki [19]; Severt et. al. studied different two ion fragmentation processes of formic acid [30].

Ionization of molecules can lead to fragmentation processes. By studying the momenta of these fragments knowledge about ionization and dissociation processes is gained. The development of COLTRIMS (COLd Target Recoil Ion Momentum Spectroscopy) gave rise to this providing an imaging technique which allows full angle resolved momentum spectroscopy and coincidence measurements [25]. In a so called Reaction Microscope charged fragments as electrons and ions that are released after ionization of a cold gas jet can be detected.

In this thesis experiments done with methane CH_4, best known for being the main compound of natural gas and as a strong greenhouse gas, are analyzed. With a femtosecond pulsed laser single pulse and pump-probe experiments were done using a Reaction Microscope. In the first part of the thesis theoretical background to important concepts of ionization in strong laser fields as well as to dissociation processes of molecules is given. This is followed by a description of the experiment's set-up of laser and ReMi including methods for momentum reconstruction and coincidence measurements. The main part will then focus on two body dissociation processes. Different fragmentation channels will be analyzed and discussed. The results are then summarized in the last chapter. For simplification many calculations in atomic and molecular physics are done in Hartree atomic units (a.u.). An overview about this system of

units and its correspondence to SI units is shown in appendix A.

2 Theoretical Background

2.1 Photoionization

Over 100 years have passed since the groundbreaking experiment of the photoelectric effect by Heinrich Hertz in 1887 [14] and its theoretical explanation by Albert Einstein in 1905 [7]. The introduction of photons explained the observation that only light of short enough wavelength was able to dislodge electrons out of a material. The development of the first lasers in the 1960s made another method possible [23]. High intensities can be used for photoionization to compensate that the photon energy is smaller than the ionization potential. By using pulsed lasers and shortening their duration into the femtosecond regime, very high intensities I can be created in such a pulse.

Ponderomotive Potential

An electron in a strong oscillating electric field is expected to follow the force provided by this, leading to an oscillation of the electron. Using the classical equation of motion of such a harmonic oscillator

$$m_e \frac{\mathrm{d}v}{\mathrm{d}t} = eE_0 \cos \omega t, \tag{1}$$

one can calculate the oscillation amplitude x_0 to [16]

$$x_0 = \frac{e\lambda^2}{4\pi^2 c^2 m_e} \sqrt{\frac{2I}{\epsilon_0 c}}. \tag{2}$$

The average energy to this quiver motion is then called the ponderomotive potential U_p:

$$U_p = \left\langle \frac{1}{2} m_e v^2 \right\rangle = \frac{1}{4} m_e \omega^2 x_0^2 = \frac{e^2}{8\pi\epsilon_0 c^3 m_e} I\lambda^2, \tag{3}$$

where for the last step 2 was used. For a central wavelength of 800 nm of a commercial Ti:Sapphire laser with an intensity in the focus of about $3 \times 10^{14}\,\mathrm{W\,cm^{-2}}$ the ponderomotive potential experienced by the electron would be 17.9 eV.

Applying this to a bound electron in an atom, we have to consider than an electron in an electromagnetic field also shows shifts of its energy eigenstates due to the laser field. For an oscillating electric field the AC Stark shift is relevant, dependent on the intensity of the field. In fact for such high intensities it is a dominating effect. In the high-frequency limit the Stark shift exactly matches the ponderomotive potential derived above [16]. The ionization potential I_P is then increased by the ponderomotive potential to $I_P(I) = I_{P,0} + U_p(I)$.

Keldysh Parameter

Ionization in strong laser fields shows different possible processes. Clearly, for visible or near-infrared lasers, ionization of an atom or molecule due to absorption of one single photon is not possible; the photon's energy is just too low (about 1.55 eV for 800 nm wavelength). Now, different processes can appear. First, by absorption of multiple photons, the ionization energy can be reached. Second, due to the strong laser field the atom's potential can be deformed that strongly that the atom can tunnel out of the Coulomb barrier. Both processes will be described in the later paragraphs. To have an estimate for the strength of the laser field the Keldysh parameter is used, introduced by Keldysh in 1965 [20]. It

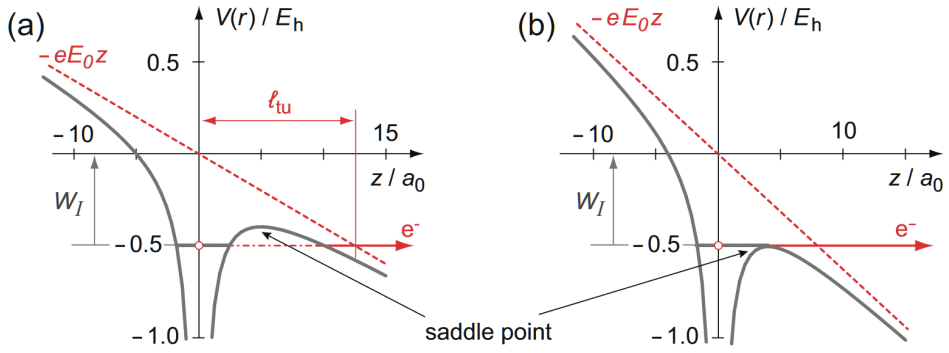

Figure 1: Ionization processes in very intense laser fields. In a) the potential is tilted by the electric field to the extent that the electron can tunnel out of the atom. In b) it is even enhanced so that the electron is emitted above the barrier. Taken from [16].

shows the ratio between the zero-field ionization potential $I_{P,0}$ and the ponderomotive potential U_p

$$\gamma = \sqrt{\frac{I_{P,0}}{2U_p}}. \tag{4}$$

Values larger than 1 indicate a dominant Coulomb potential, while $\gamma < 1$ would rather mean that the laser field is stronger than the atomic field [16]. In other words, the Keldysh parameter gives an estimate if the ionization process is dominated by multi-photon-absorption ($\gamma > 1$) or by tunneling ($\gamma < 1$). However, especially for molecules this parameter is rather inaccurate, because the deviation of the parameter is completely independent of the actual shape of the potential the electron is in. For molecules, the very different potential shapes can produce significant errors [6].

Multi-photon ionization

Absorption of several photons is a quite complicated process. In the simplest case lowest-order perturbation theory is used [13]. This means that for absorption of a number of N photons, the lowest non-vanishing term is of Nth order. Thus for low intensity fields multi-photon ionization is strongly suppressed and pulsed lasers are needed. The ionization probability depends on a generalized ionization cross section $\sigma^{(N)}$ as well as the photon flux $\Phi = I/(\hbar\omega)$. In lowest order perturbation theory the transition rate can be written as [16]

$$R^{(N)}_{k_e \leftarrow a} = \sigma^{(N)} \Phi^N \tag{5}$$

from a bound state $|a\rangle$ into the continuum state $|e\rangle$. It is also possible that more photons are absorbed than actually needed for ionization. This so called above-threshold ionization [1] leads to higher energetic electrons with an additional energy of $M\hbar\omega$ with M the number of additionally absorbed photons. The angular distribution of the emitted photoelectrons then also changes since a photon also gives an angular momentum kick of $\pm\hbar$ to the electron.

Tunneling ionization

However, for very intense laser fields, saturation begins, meaning almost all atoms in the laser focus are ionized. The approach described above looses validity then. Also when the inner atomic and the electrical field are of comparable strength tunneling ionization becomes relevant. The electrical field disturbs the Coulomb potential in a way that photons can escape from the potential by tunneling through the barrier.

In this image, the λ^2 dependence of the ponderomotive potential gets a new vivid explanation. If the laser field is oscillating slower the electron has more time to tunnel out of the potential. In a more extreme case the potential is disturbed even more so that the electron is simply free to move out, a so called above barrier ionization. Both processes are shown in figure 1. For quantifying tunneling ionization processes *ADK-theory* is often used, named after the three authors of the first publication in 1986 [3]. It assumes that saturation, meaning all atoms in the laser focus being ionized, starts at that point, when the field strength is high enough to allow for above barrier ionization. For more information about the exact formula and its derivation see the original paper [3].

2.2 Dissociation of molecular ions

Ionization of molecules enables complex dynamics of the molecule. Vibrations and rotations can be excited, changing electronic wave functions can lead to changing intermolecular distances and structure deformations. It is also possible that the molecule dissociates. A short theoretical insight is given in the following sections – general and for methane, the molecule of interest, specifically.

Franck-Condon-Principle

The Franck-Condon principle explains changes of vibrational states due to electronic transitions in molecules. This holds obviously also for ionization processes in molecules. The main principle is the well known Born-Oppenheimer approximation stating the electronic wave function changes on a much faster timescale than the nuclear wave function does [5]. This means that the nuclear wave function and so the internuclear distance can be assumed to be constant during the ionization process. The change of the electronic wave function thus happens vertically in the so called Frank-Condon region. The new wave function then has a new potential minimum for a certain distance of the nuclei which they will reach in the following. With ionization also rotational and vibrational modes can change. The energies of those modes lie in the range of some meV for rotational modes and in the range of some 100 meV for vibrational modes. Assuming that initially all molecules are in vibrational ground state this means that a relevant part of the energy during photoionization can be stored in the excitement of such vibrational modes. The calculation which modes are preferably excited during photoionization is very complicated, especially for larger non-linear molecules. In a simple model of a diatomic molecule one can show that the transition probability is in first order proportional to the overlap integral between the vibrational wave functions of the potentials before and after ionization [17]. In other words transitions are most probable to that vibrational state which has the highest wave function overlap with the initial wave function.

Dissociation

Not every potential curve has a stable minimum at a certain internuclear distance. In the simplest case of the $H_2{}^+$ molecular ion shown in figure 2, the two lowest states are the bonding $1s\sigma_g$ and the anti-bonding $2p\sigma_u$ molecular orbital (MO). Ionizing to the $1s\sigma_g$ MO will lead to a stable $H_2{}^+$ ion, while the $2p\sigma_u$ MO has no potential minima at finite internuclear separation leading to a dissociation of the molecule. Thus dissociation is possible by excitation of the $1s\sigma_g$ to the $2p\sigma_u$ state. Several pathways are possible, for example by absorption of another photon to the anti-bonding MO. This is strongly enhanced for exactly this nuclear distance where the energy difference between the two MO matches the photon energy. This resonant one photon excitation is thus also possible at comparatively low laser intensities at the pulses tail and will lead to a dissociation of the molecule in to $H^+ + H^0$. Such an one-photon transition is enhanced when the molecule is oriented along the lasers polarization axis. Then the transition dipole

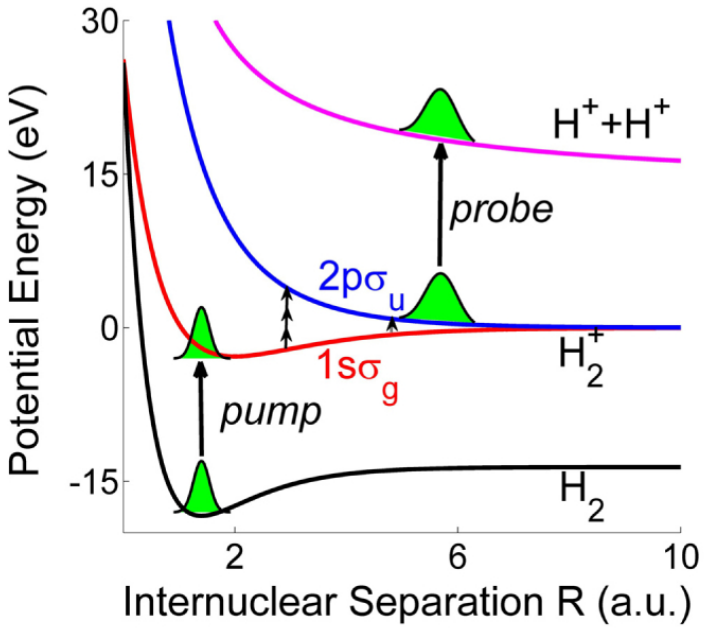

Figure 2: Dissociation process of H_2 in a pump-probe experiment. After ionization the molecule can reach the dissociative $2p\sigma_u$ molecular orbital ${H_2}^+ \longrightarrow H^+ + H^0$ by absorption of another photon. A possible three-photon absorption is also drawn. Eventually the probe pulse further ionizes the neutral H^0 fragment leading to a Coulomb explosion curve. Taken from [26].

moment is maximal while it is zero for the molecules' dipole moment being orthogonal to the polarization axis.

Coulomb explosion

The term Coulomb explosion refers to dissociation processes with two (or more) ionized fragments formed in which the fragments receive high kinetic energies. In the easiest case as above for H_2 two electrons are removed leaving a hypothetical molecule consisting of two protons. Clearly no further force than just the repulsive Coulomb-force will act on them resulting in a highly energetic, explosion like dissociation pathway. The kinetic energy release (KER) of this process is

$$E_{\mathrm{KER}} = \frac{q_e^2}{4\pi\epsilon_0 r_0} \tag{6}$$

and only dependent on the initial internuclear distance r_0. This process can either be direct without an intermediate state or in a pump-probe experiment with two laser pulses as shown in figure 2. The first laser pulse singly ionizes the molecule to the $1s\sigma_g$ state of ${CH_4}^+$. In the following time the molecule travels along this potential curve towards larger internuclear distance and being able to resonantly absorb another photon to the anti-bonding MO as in the dissociation case. After some delay time the second laser pulse ionizes the atom further leading to a Coulomb explosion. In equation 6 the radius of the $\frac{1}{r}$-potential has to be changed to the new time-delay dependent radius $r_M(t)$ at which the second ionization takes place. Additionally the KER has to be extended by a second term including the kinetic energy of the nuclei before the probe pulse as well as the energy stored in vibrational degrees of freedom.

2.3 Methane molecule

Experiments with methane were analyzed in this thesis. Methane (CH_4) is a quite simple polyatomic molecule due to its highly symmetric arrangement. Additionally it is the shortest alkane and the easiest organic compound. Methane shows a binding angle corresponding to its tetrahedral structure of 109.47° and an equilibrium bond length of 1.087 Å [15]. Out of this, also the distances of the centers of masses between individual fragments as $CH_3 + H$ and $CH_2 + H_2$ in the electronic and vibrational ground state can be calculated. This leads to a CH_3–H distance of about 1.185 Å and for CH_2–H_2 to a distance of 0.717 Å.

The carbon atom has an electron configuration of $(1s)^2(2s)^2(2p_x)(2p_y)$. For allowing 4 chemical bonds one 2s electron has to be moved into the unoccupied 2p orbital creating 4 singly occupied molecular orbitals. This reorganization requires energy but is overcompensated by the energy gain due to the binding with the H-Atoms. By using hybrid atomic orbitals one can then create 4 equivalent sp^3-hybridized atomic orbitals. This is done via linear combination of atomic orbitals

$$|1\rangle = \frac{1}{\sqrt{4}}\Big(|2s\rangle - |2p_x\rangle + |2p_y\rangle + |2p_z\rangle\Big)$$

as an example. The binding then results in the overlap of these new wave functions with the 1 s atomic orbital of hydrogen. This ansatz can actually explain the tetrahedral T_d structure of methane well but fails in giving an idea about the binding energies of the electrons. Due to orbital hybridization one would expect all valence electrons to be bound equally strong. However, experiments show clearly that there are two electronic levels. One stronger bound molecular orbital $(2a_1)^2$ and one triple degenerate $(1t_2)^6$ state. The CH_4 molecule is thus better described by a $(1a_1)^2(2a_1)^2(1t_2)^6$ configuration which shows a close relation to the Neon configuration $(1s)^2(2s)^2(2p)^6$ [33]. Ionized states are affected by Jahn-Teller distortion [18]. The Jahn-Teller effect states that non-linear molecules show instability towards degenerate electronic states. With one electron removed from the $1t_2$ shell a triple degenerate state is obtained. This degeneracy is removed by symmetry breaking leading to a lowering of the total energy for the new ground state.

All this becomes important when looking at energy spectra of ionized methane as figure 3 shows. Two ionized configurations exist for ${CH_4}^+$ depending which electron was removed. The energy difference is with about 10 eV significant. The energy needed to remove one of the $2a_1$ valence electrons is much higher than for many dissociation processes. Most important to mention are the ones which split in two fragments ${CH_3}^+ + H^0$, ${CH_3}^0 + H^+$, ${CH_2}^+ + {H_2}^0$, ${CH_2}^0 + {H_2}^+$ with energies of about 14 eV to 20 eV. Ionization leaves the methane molecule in a ${}^2T_2$ ground state still with tetrahedral symmetry. However, due to Jahn-Teller distortion the ${}^2T_2$ state itself is split into three states of a lower but different symmetry [28].

For double ionized methane Coulomb explosion processes are much more difficult than in the simple ${H_2}^+$ case. Many studies, experimentally [10] [34] [29] and theoretically [35] [10] [34], have been done to get information about its structure and stability. Not only there are different final fragments to consider (${CH_3}^+ + H^+$, ${CH_2}^+ + {H_2}^+$, etc.) but also different structural configurations. As already shown in 1981 direct photoionization can lead to methane dications with a quite long lifetime of several µs, but also Coulomb explosion like processes with a lifetime in the fs range were observed in other experiments at that time [4]. In 1989 Wong and Random proposed with their calculations that the structure of ${CH_4}^{2+}$ ground state is – again due to Jahn-Teller distortion – preferred to be planar with two long and two short

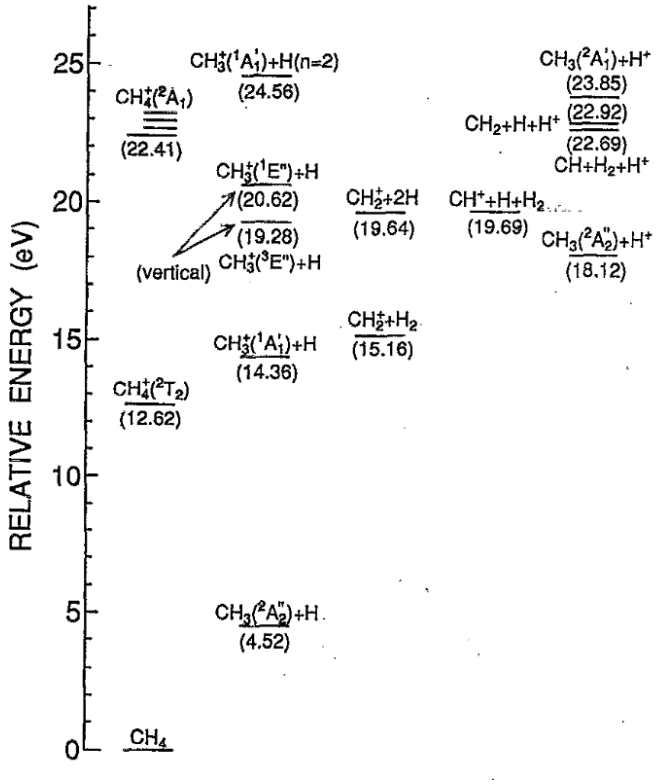

Figure 3: Energy level diagram for different singly ionized dissociation pathways. The energy splitting of $CH_4{}^+$ depending on which electron was ionized can be seen clearly. The corresponding symmetry group is shown in brackets for the $CH_4{}^+$ and $CH_3{}^+$ fragments – splittings due to Jahn-Teller distortion are not shown. Taken from [12].

C–H bonds (C_{2v} symmetry) [35]. A newer theoretical calculation of the dissociation channel $CH_3{}^+ + H^+$ shows different dissociation curves for different structures of the remaining methyl cation ($CH_3{}^+$). For a larger $CH_3{}^+$–H^+ distance of the two fragments – so to speak a further proceeded dissociation – a planar geometry of $CH_3{}^+$ with 3 HCH angles of 120° is lowest in energy. For small distances other configurations are energetically best. Conical intersections between those as two potential energy curves cross also play a role allowing different dissociation pathways [34].

3 Experimental setup

In this part the setup used for this experiment is described. A femtosecond pulse laser is employed and guided into a reaction microscope (ReMi). There the laser is focused into a supersonic gas jet. By applying electric and magnetic fields the ionized fragments can be directed to time and position sensitive detectors. Their output can then be used to get information about the appearance and structure of different reaction pathways.

3.1 Femtosecond pulse laser

A commercial Ti:Sapphire pulse laser system is used and then adapted to compress the pulse further. The laser system contains an oscillator, an amplifier and a compressor. In the oscillator a weak pulsed laser beam is generated and then stretched in time. Afterwards the pulses get amplified by passing several times through a Ti:Sapphire crystal and finally get compressed again by using chirped mirrors and prisms. The final 25 fs long pulses with an energy of 1 mJ are centered at a wavelength of 800 nm corresponding to a photon energy of 1.55 eV with a repetition rate of 3 kHz. A more detailed description of the laser system can be found in [11].

In order to make the pulses even shorter, one has to broaden the spectrum first. This is done by using a hollow-core-fiber filled with 0.5 bar of Argon. Due to the high intensities of the laser, the optical Kerr-effect plays a role with an intensity-dependent refractive index $n(I)$

$$n(I) = n_0 + n_2 I. \tag{7}$$

This concept known as self-phase-modulation produces a variation in the temporal phase leading to a broadening of the spectrum.

For the compressing part a setup of holographic gratings (HG) and a spatial light modulator (SLM) is used. HG are diffraction gratings made out of a gelatin material with a sinusoidal refractive index, leading to a spectral separated pulse. The pulse is then collimated by a cylindrical mirror (CM) and guided to the SLM. The same holds for the way back, when the spectral broadened beam is recombined again by a CM followed by a HG. A sketch of this setup can be found in figure 4a. The configuration is in a so-called 4f-geometry, meaning that the distances between HG and CM, CM and SLM, as well as for the way back, all match the focal length of the cylindrical mirror.

A SLM contains two identical liquid crystal screens each consisting of 640 liquid crystal layers with electrodes to steer individually. In figure 4b such a layer of liquid crystals is shown between two glass plates. Inside the glass plates electrodes and an alignment layer is placed for the spatial modulation of the liquid crystal molecules. Without an electric field the molecules are all aligned parallel to the glass plates. By now applying an electric field, the orientation of the liquid crystal molecules can be changed. Due to their behavior as a birefringent material, the optical axis and thus the refraction index is also changed. This is done for each electrode individually, allowing different adjustments for different frequency components. With this setup the pulse can be compressed further in time and dispersion caused by spectral broadening in the hollow-core-fiber is compensated. The steering is done by an evolutionary algorithm program which determines the best voltage settings.

Additionally, the SLM gives the possibility to split the pulse into two identical ones, allowing pump-probe experiments. With varying voltages the time delay between two pulses can vary smoothly over the range.

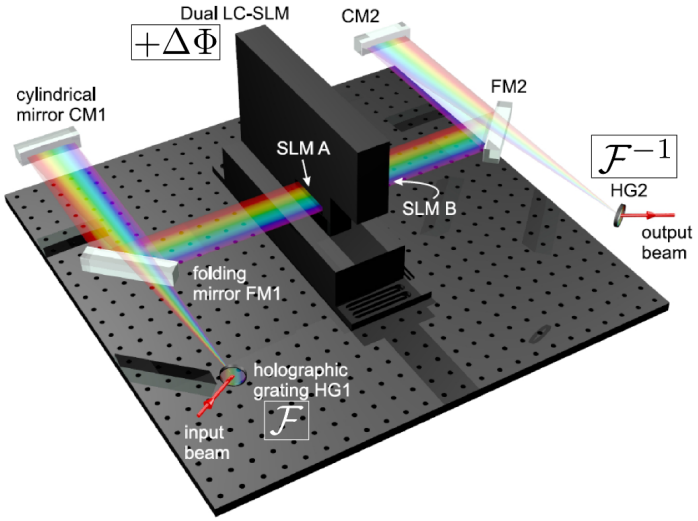

(a) 4f-construction the Spacial-Light-Modulator is embedded in. The distances match exactly the focal length of the cylindrical mirrors. Taken from [11]

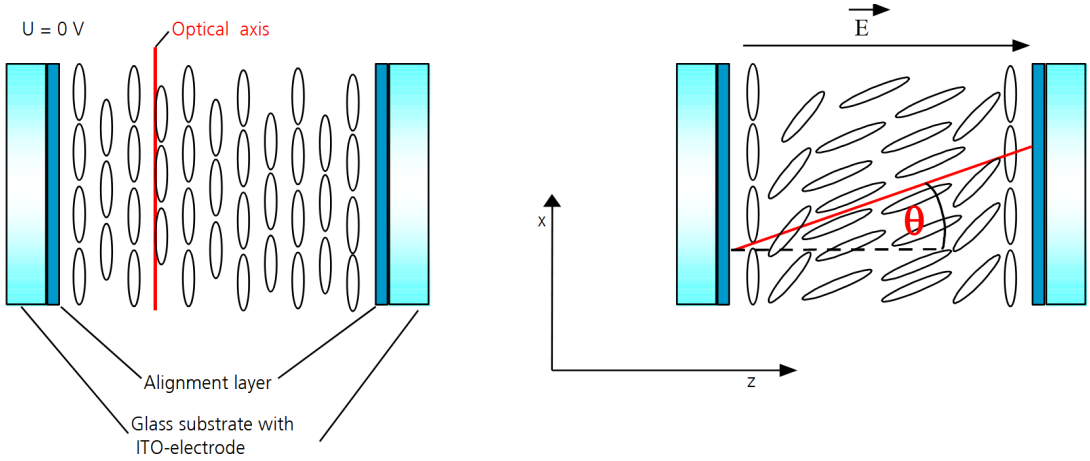

(b) Profile of one liquid crystal layer. Left without an electric field. Applying a voltage leads to a tilting of the molecules (right). Taken from [24]

Figure 4: Setup of the SLM and its implementation into the laser. With this construction the laser pulses can be shaped.

In the pump-probe experiment done here, the delay was varied from -50 fs to 1000 fs. The width of one single pulse can be lowered to around 12 fs.

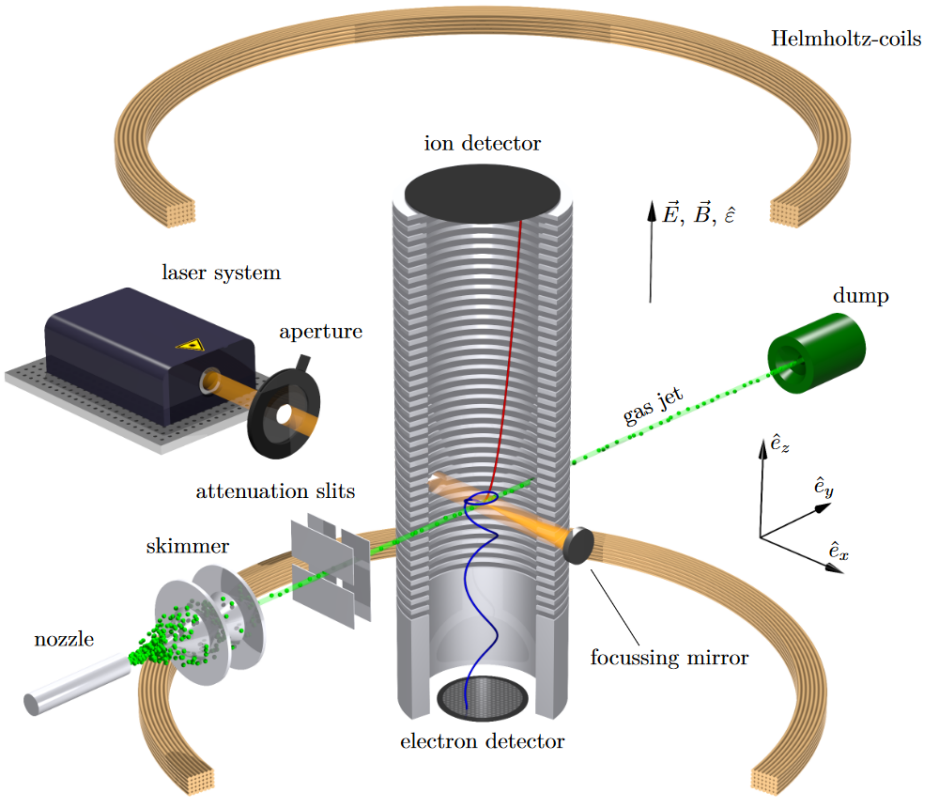

Figure 5: Schematic setup of the ReMi. Important parts are labeled and explained in the text. Ion's curve in red, electron's curve in blue. Taken from [9]

3.2 Reaction Microscope

Reaction Microscopes are instruments for the detection of ionized fragments from reactions of atoms or molecules. With their setup time and angle resolved measurements can be done making it suitable for precise coincidence measurements. Figure 5 shows a schematic drawing of the ReMi's setup used in this work. The pulsed laser is aligned into a vacuum chamber, in which it is focused into a supersonic gas jet.

Supersonic beam

The molecular beam is produced via supersonic expansion. Therefore the gas (in the experiment CH_4 with a gas pressure of 1.8 bar) is released into the jetline through a small nozzle with a diameter of about 50 µm. Due to the large pressure difference before and after the nozzle, the directed momentum in jet direction increases to a supersonic velocity. Thermal energy thus gets reduced which leads to a cooling of the jet. In other words, the velocity spread of the molecules is strongly reduced. This is highly necessary because for the later momentum reconstruction it has to be assumed that all molecules are flying with the same velocity. From this assumption it is followed that the spatial difference from the main detection spot is only caused by the momentum gain from the interaction with the laser. The jetline itself is divided into several differential pumping stages with small tubes between each, allowing the jet to pass. This structure makes it possible to lower vacuum at each stage, so that in the main chamber where the interaction with the laser takes place the pressure reached values of 3×10^{-10} mbar during the analyzed measurement. Afterwards the unionized molecules are travelling further into the dump chamber where they are pumped out.

The laser needs to be aligned with the opposing mirror, so that the point where the laser beam crosses the jet is exactly the focal point of the mirror creating intensities as high as possible. In the beam focus this can reach around $3 \times 10^{14}\,\mathrm{W\,cm^{-2}}$.

Spectrometer and detectors

In the center of the ReMi the pulsed laser is focused into the gas jet so that molecules get ionized and break up. Around this a spectrometer consisting of several ring electrodes is mounted. A picture of this is shown in figure 6. With this structure a homogeneous electric field is created accelerating positively charged ions upwards and electrons downwards. For electrons an additional drift zone with no electric field is included. After this ions and electrons hit the detector. The detector consists of two microchannel plates (MCPs) followed by a delay line anode. A MCP is made up of millions of single tubes having an inner diameter of about 12 µm each. They are slightly tilted such that incoming high energetic particles are able to remove electrons from the tube wall. A voltage of around 2 kV is applied between front and back of the MCP accelerating the removed electrons, so that the single tube is acting as an electron multiplier. With this the time of flight (ToF) of the charged particle can be measured as the time difference between laser pulse and MCP hit. Behind the MCP a delay line anode is installed for a position sensitive detection of the electron cloud. Such a delay line anode consists of a plate with two copper wires tightly wound around them - one in x and one in y-direction. When an electron cloud now hits the delay line, a signal in form of a voltage peak can be measured at both ends of each wire. With the time difference between the two arriving signals of one wire, the position of the original particle can be calculated. However, the sum of both x-signals has to be constant due to the constant length and travelling velocity of the charges along the wire. Thus, this sum is used to measure more than one incoming particle per laser shot and also to rule out the signals where the x-component was measured wrongly. The same holds for the y-position. Using this setup, up to three ions and three electrons can be measured per laser shot, giving the possibility to analyze up to three body breakups in coincidence.
Additionally, a magnetic field is applied. Two Helmholtz coils located outside of the vacuum chamber are used to create a homogeneous magnetic field inside of the spectrometer. While ions are barely influenced by this due to their large mass, electrons are diverted due to the Lorentz force flying on a cyclotron trajectory. With this method the electrons can be focused onto the detector preventing them to fly out of this range.
In figure 7 the resulting ion and electron positions are shown after the time difference of the signals was converted into a position in mm and after removing those event where the sum of both signals did not match. The direction of the laser beam is labeled the x-direction, while the jet's direction is labeled with y. Two important things can be already seen here. Firstly, at the ion detector image the main intensity peak is shifted downwards in y-direction. This is due to the velocity of the molecules in the jet and has to be taken into account when later calculating the momentum. Secondly, especially the ion detector is not centered corresponding to the interaction zone of jet and laser. Whether an ion is detected or not because it is outside of the detector range is thus not only dependent on the amount of transversal momentum, but also on the angle in the transversal plain.

Figure 6: Image of the spectrometer in May 2023. The two visible holes in the spectrometer show the openings for the laser (small) and jet (large). The ions are accelerated to the top, the electrons to the bottom. The drift region for electrons is also seen well. Above the spectrometer, two MCPs and the delay-line-anode for ions is mounted. Copper cables are used for applying voltages and receiving signals from MCP and delay-line.

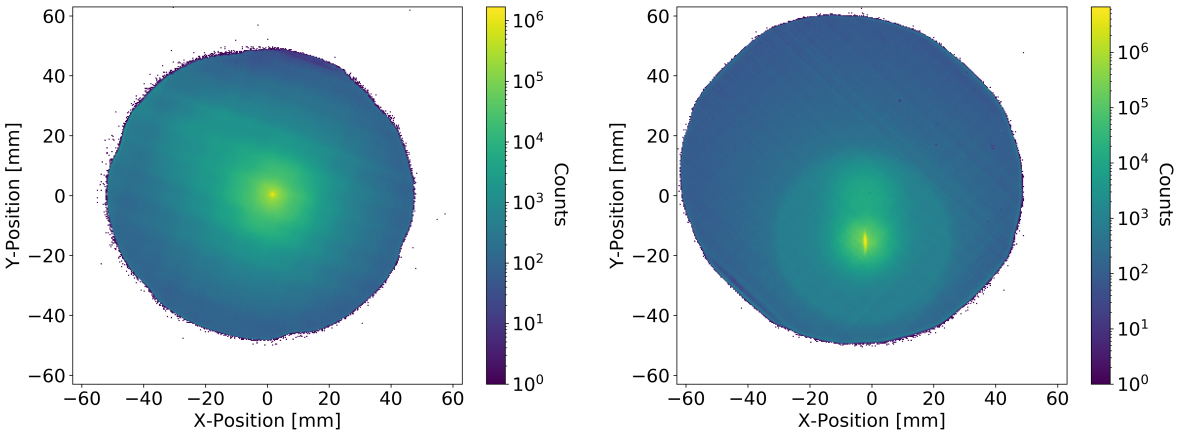

(a) electron detector (b) ion detector

Figure 7: Resulting image from both detectors. The jet direction is visible as well as that the detectors are not centered.

3.3 Momentum reconstruction

With information on the time of flight and detector position, the initial momentum of the charged fragments can be detected. In this thesis only ions were investigated, thus this calculation is only done for them. For electrons it is similar; however also the drift zone as well as the magnetic field have to be included which makes calculation more complicated.

Longitudinal momentum component

The initial longitudinal momentum $p_l = p_z$ along the spectrometer axis is dependent on the time of flight t and the ions mass m:

$$s = \frac{1}{2}at^2 + p_l\frac{t}{m}. \tag{8}$$

The acceleration a is due to the Lorentz force of the homogeneous electric field E. Setting this into equation 8 one can solve for the initial momentum and get

$$p_l = m\frac{s}{t} - \frac{1}{2}Eqt, \tag{9}$$

where s is the length of the acceleration path which is for ions 30 cm.
However, the time of flight measured at the MCP is not exactly the one of the particles. Due to the data acquisition process an additional systematic delay time t_{sys} has to be included. For a particle with zero longitudinal momentum this means that

$$t_{meas} = \sqrt{\frac{2sm}{Eq}} + t_{sys}. \tag{10}$$

One can see that different particles will show a different ToF according to the root of their mass to charge ratio. A ToF spectrum of CH_4 is shown is figure 8. Fragments can be identified with the peaks and their exact peak position can be used to fit a curve 10 obtaining an estimation for t_{sys}. In case of the methane experiment done here, the peaks of H^+, $CH_4{}^{2+}$, $CH_4{}^+$, $^{13}CH_4{}^+$ and H_2O^+ were used. Due to the divided structure of H^+, the minimum between the two central peaks was used.

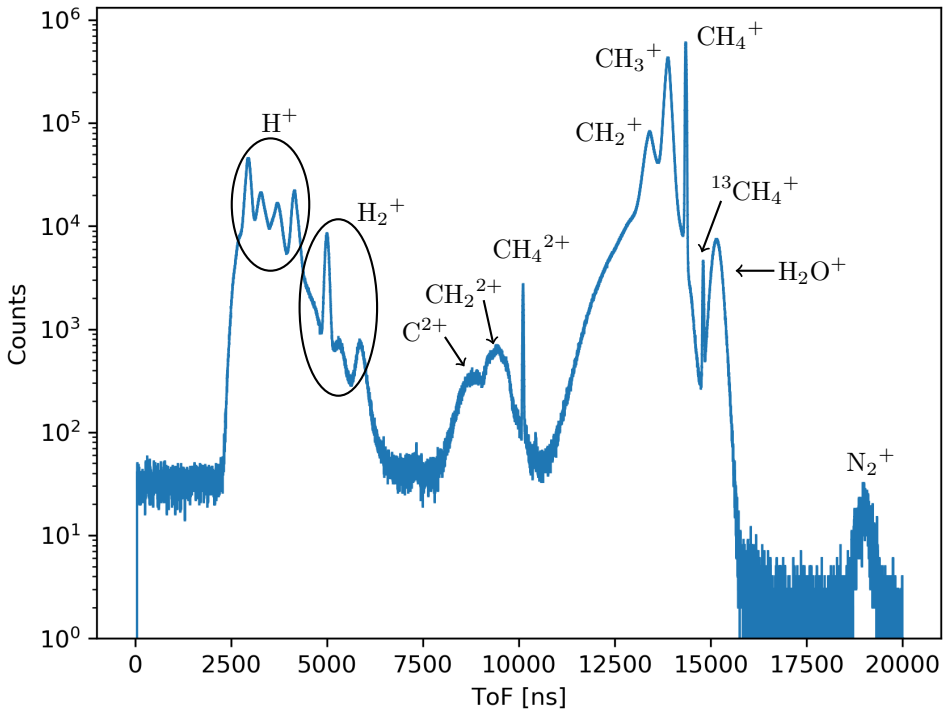

Figure 8: Time of flight spectrum of a pump-probe measurement done with methane (CH_4) with logarithmic ordinate. Identified peaks are labeled. Peaks of the spectrum are used to get an estimate for the systematic delay of the detection process.

The goal of interest is to select those fragments which descend from the same dissociation process. Because only charged fragments can be measured directly, the focus will lie on the breakup of methane into two ions. For this breakup momentum conservation holds and huge amounts of energy will get free. Especially, this energy is much larger than the initial recoil momentum from the ionization because the electron mass is more than thousand times smaller than the ion mass. Using momentum conservation and equation 9, a formula for the time of flight of the second ion can be derived [32]:

$$t_2(t_1) = \frac{1}{q_2}\left[\sqrt{\frac{s^2}{U}\left(2m_2q_2 + \frac{m_1^2 s^2}{t_1^2 U} - m_1 q_1\right) + \frac{1}{4}t_1^2 q_1^2} + \frac{s^2}{U}\frac{m_1}{t_1} - \frac{1}{2}t_1 q_1\right], \tag{11}$$

where $U = Es$ is the voltage applied to the spectrometer.

Figure 9 shows an example of such a coincidence line for the breakup into CH_3^+ and H^+. Horizontal and vertical lines show wrong coincidences of particles originating from two different fragmentation processes, other bent lines originate from other Coulomb explosion processes. By now slightly correcting the estimated values of s and t_{sys}, equation 11 can be fitted along the data and the true coincidences can be extracted.

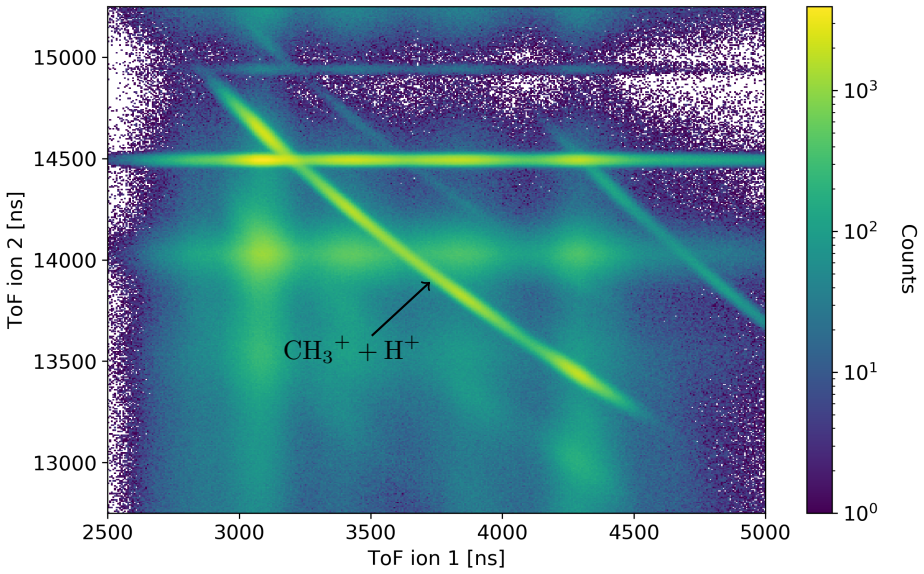

Figure 9: Example of a coincidence line between CH_3^+ and H^+.

Transversal momentum component

For the transversal momentum p_t the positions of the detector are needed. However, as already mentioned it is necessary to correct for the velocity of the jet. This is done by centering the main peak of each molecular species with respect to the zero position of the coordinate system. If the influence of the magnetic field is neglected, the momentum calculation is then straight forward and leads to

$$p_t = \frac{\sqrt{x^2 + y^2}m}{t}. \tag{12}$$

4 Data analysis

For this thesis an experiment done with methane (CH_4) was analyzed. A pulsed laser of 800 nm central wavelength corresponding to a photon energy of 1.5 eV was used. Two measurements were done, one single pulse experiment and a pump-probe experiment. The laser pulses were shortened to a duration of about 12 fs. For the pump-probe experiment the pulse was spitted into two parts; one of them was then delayed by a varying time interval of up to 1 ps. For detection a Reaction Microscope (ReMi) was used as explained in the previous section. In this chapter the results of two body breakups of CH_4 are presented and discussed. After a small introduction, the first part will show dissociations in a single pulse experiment with only one charged fragment. Because neutral fragments will not be detected with this ReMi, the larger focus will rely on breakups with two ions detected in coincidence with each other. With the use of a second pulse in a pump-probe measurement, an additional channel appears which is highly dependent on the time delay between both pulses. The focus of this work lies on a comparison of different breakup channels of methane.

In figure 10 the ion's ToF is plotted against the y-position of the detector, corresponding to the jet direction. Assuming a neglectable temperature and thus every molecule to have the same initial velocity, the molecules originating from the jet are shifted towards positive y-direction. This linear shift with rising ToF is clearly seen in the plot. However, some peaks do not follow this behavior. In perfect vacuum all detected events would originate from CH_4 fragmentation. This is obviously impossible, so there is always some residual gas in the chamber moving through the laser focus with no directed velocity. Hence the central detection point is not shifted in y-direction. Unsurprisingly the residual gas is made up of water and nitrogen visible at larger ToF, but also molecular hydrogen. H_2 originates from outgasing of the vacuum chamber and is, due to its small mass, hardly pumped out by turbomolecular pumps used in ultra-high vacuum. Therefore the inner peak of $H_2{}^+$ at 5000 ns is difficult to assign. Ionized residual hydrogen is possible as well as molecular hydrogen as a fragmentation product of CH_4 with low kinetic energy. The inner peak has a high intensity compared with other hydrogen fragments in the spectrum and the y-position is about the same as for residual H_2O. Thus, it is unlikely that all this originates from CH_4 dissociation and residual gas is a probable source.

The extension of the spots is mainly due to their momentum gain after ionization and dissociation. Non surprisingly the spots for both $CH_4{}^+$ isotopes at 14 300 ns and 14 800 ns are sharply localized; the recoil energy from ionization is comparably small. For H^+ from 2500 ns to 4500 ns and $H_2{}^+$ from 4000 ns to 6000 ns, there are two ring structures belonging to direct and indirect Coulomb explosion processes. Also for $CH_3{}^+$, centered at 14 000 ns, a Coulomb explosion ring is visible which is partly overlapping the central $CH_2{}^+$ spot at 13 500 ns. Doubly ionized fragments of methane are detected between 8000 ns and 10 500 ns.

The existence of molecular hydrogen ions as a product of CH_4 fragmentation is itself an interesting topic. As initially no hydrogen is bound together in methane, it has to be formed during dissociation. In this dissociation process two C−H bonds have to be broken and one new bond between the two hydrogen atoms established by sharing one electron to form $H_2{}^+$.

Finding coincidences of two charged particles is possible via observing the time of flights of two ions originating from the same laser pulse with respect to each other. Such a time of flight correlation spectrum can be seen in figure 11. Events are located only in the upper triangle of the spectrum because the ion with the lower ToF is always considered to be the first one. False coincidence lines are quite

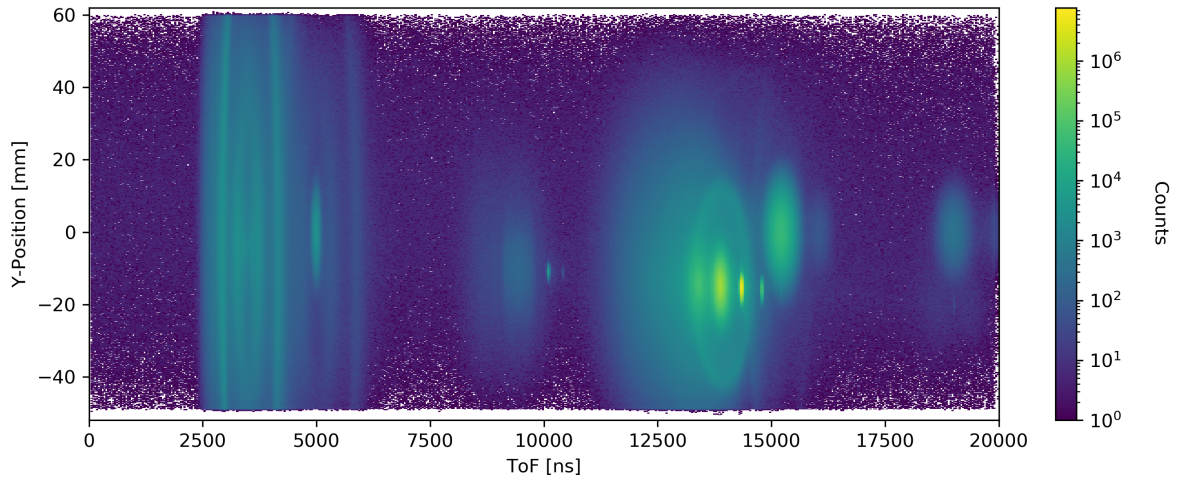

Figure 10: Time of Flight versus y-position on the detector in a pump-probe experiment. For gas jet molecules the y-position changes linearly with the ToF. Ionized molecules from background gas are primary $H_2{}^+$,H_2O^+ and $N_2{}^+$. Large ellipse structures originate from dissociation and coulomb explosion processes.

prominent and can be identified using the peaks of the ToF spectrum from figure 8.

As discussed in chapter 3.3, true coincidences between two particles appear as slightly bent lines in the spectrum. The length of those lines corresponds to their initial amount of momentum in longitudinal direction. Most prominent to observe are the ones for $CH_3{}^+ + H^+$, respectively $CH_2{}^+ + H_2{}^+$. For those lines count rates are high enough that a further analysis makes sense. Non-surprisingly a second parallel line shifted slightly upwards for the ^{13}C-isotope is also visible. Interestingly the $CH_3{}^+ + H^+$ line is elongated up to the point where the two false coincidence lines of $CH_4{}^{2+}$ meet. This shows that there is another Coulomb explosion channel where the breakup into two molecules is delayed. This implies that there is a metastable $CH_4{}^{2+}$-state with a comparatively long lifetime.

Additionally Coulomb explosion fragments from a triple-ionized ion were detected. The most prominent one is the one of $CH_2{}^{2+} + H_2{}^+$. Additionally, in the range of two hydrogen atoms some coincidence is seen. Possible are three body breakups into $CH_2{}^+ + H^+ + H^+$, where only the first two hydrogen atoms are in the coincidence plot. To analyze those other methods have to be used, which also include the ToF of the possible third ion, for extracting the events.

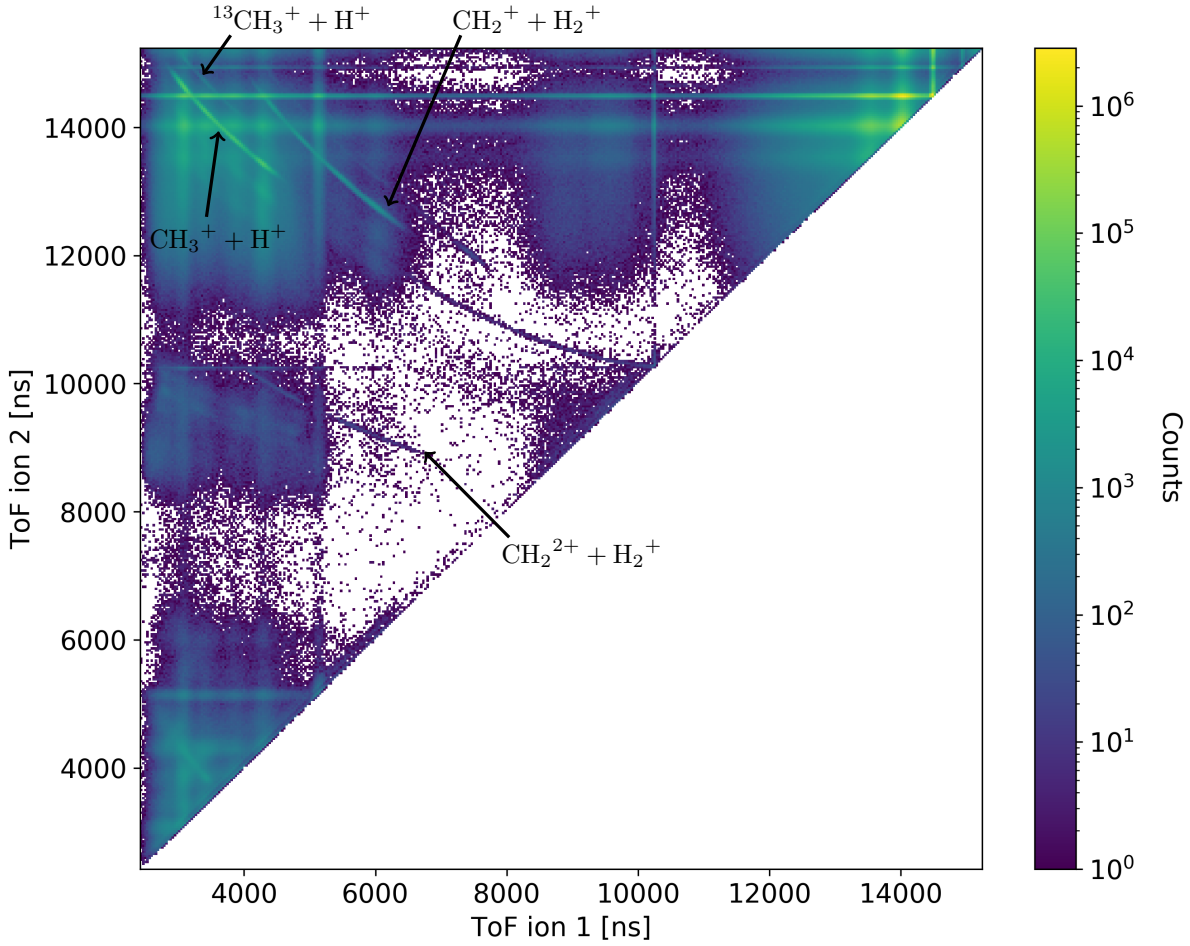

Figure 11: Time of flight coincidence plots for two ions in a pump-probe experiment. Vertical and horizontal lines show false coincidences. Visible coincidence lines are labeled in the spectrum.

4.1 Single pulse dissociation

In this part a single pulse experiment is analyzed. At first, the focus lies on single ionization followed by a dissociation of the molecule. Later, these results are used to compare them with pump-probe Coulomb explosion pathways. The extraction of such events including a charged and a neutral fragment is not possible via a coincidence measurement, because no neutral fragments can be detected. Thus the only way is to directly take the signals out of the ToF spectrum. As seen in figure 3 two body fragmentations have the lowest dissociation potential for every ion species and thus are expected to have highest count rates. Additionally, neglecting the photoelectron momentum, the momentum of the neutral fragment has to be the same as the measured ion momentum for reasons of momentum conservation. Therefore, if only two fragments exist, a qualitative analysis can work when having the momentum of the charged fragment.

For a dissociation into CH_3 three channels are expected to happen:

- $CH_4 \longrightarrow {CH_3}^+ + H^0$
- $CH_4 \longrightarrow {CH_3}^0 + H^+$
- $CH_4 \longrightarrow {CH_3}^+ + H^+$

Doubly ionized states of ${CH_3}^{2+}$ were not observed during the experiment. The third channel is showing a Coulomb explosion which will be discussed later. Thus, the focus lies on the first two dissociation channels.

Point of interest is the angular distribution of the initial momentum of both ionization channels while the laser is polarized in z-direction parallel to the spectrometer axis. Momentum conservation implies that the fragments are released back to back so it is sufficient to know the angular distribution of the charged fragment. The initial momentum is then calculated according to chapter 3.3 for longitudinal and transversal components.

Plotting the distribution of all three momentum components in one graph is not possible. For getting a visual overview over the momentum distribution, dimensions have to be reduced. The relevant axis which can show changes in the momentum distribution is the direction of the laser polarization. For a laser polarized in z-direction along the spectrometer axis, changes are expected in this direction; the x-y-plane is isotropic. Thus all momentum plots here only show the y versus z direction. The distributions for all detected ${CH_3}^+$ and H^+ fragments are shown in figure 12. The cutoff of both images has different reasons. For ${CH_3}^+$ this has just pragmatic reasons to prevent the peaks of ${CH_4}^+$ and ${CH_2}^+$ being visible in the plot. The margins of those peaks are slightly visible at top and bottom. In case of H^+ it is showing a problem that will appear several times. If the transversal momentum is too high, light ions with thus high transversal velocity will fly outside of the detection range. The slightly tilted borders are due to the fact that a negative longitudinal momentum implies that the ion has an initial momentum pointing away from the ion detector and is therefore travelling a longer time until reaching the detector. Then even smaller transversal momenta cause the ion not to hit the detector.

The ring-like structure with high initial momentum can be associated with a highly energetic Coulomb explosion of a doubly charged ion, meaning the third pathway, and will be discussed later. Channels 1 and 2 therefore show the inner distributions. Interestingly, the dissociation into ${CH_3}^+$ is not showing any angular dependence, while the one of H^+ is highly angular dependent, showing high count rates in

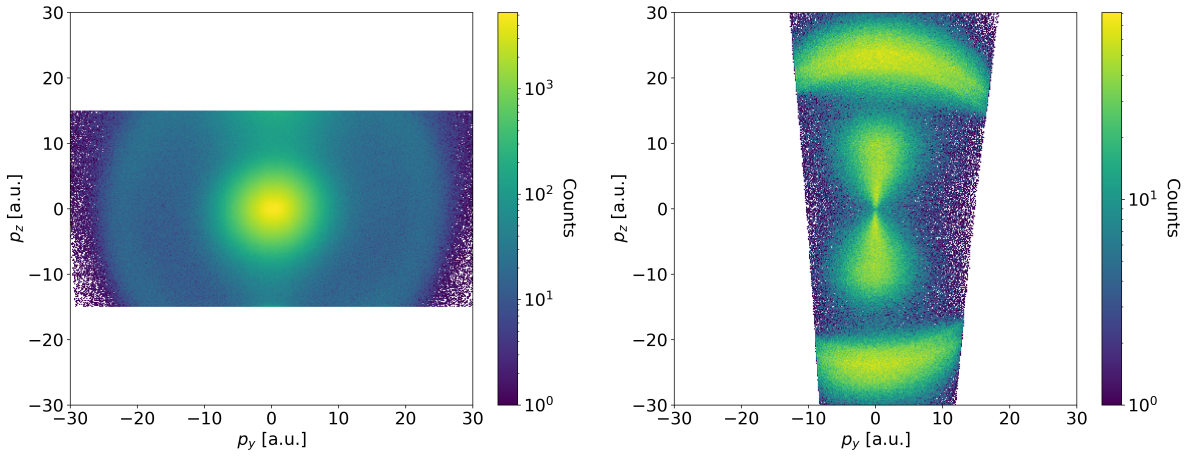

(a) momentum distribution CH_3^+

(b) momentum distribution H^+

Figure 12: Momentum in y-direction versus longitudinal momentum for CH_3^+ and H^+. The outer structure belongs to a Coulomb explosion, the inner to dissociation of singly ionized methane. Momenta given in atomic units (a.u.). The angular distribution of the two dissociation channels is clearly different.

dissociation parallel to the laser polarization. Also the absolute momentum is very different for both cases. This strengthens that the dissociation processes into $H^+ + {CH_3}^0$ and CH_3^+ and H^0 are different in their structure. Using momentum conservation and therefore assuming that the momentum of the second, neutral fragment is the same as for the charged one, the total kinetic energy release of the dissociation process can be estimated. For $CH_3^+ + H^0$ the released energy is very low and the KER-distribution shows a clear peak at around 0.03 eV. For $H^+ + {CH_3}^0$ no clear peak is visible. The kinetic energy release is equally distributed between 0 eV and 0.8 eV. The different KER-distributions could imply different steepness of the potential energy curves. The ${CH_3}^0 + H^+$ channel is showing some similarities to the H_2^+ dissociation discussed in chapter 2.2. Dissociation pathways including a dipole transition are highly dependent on the angle. Excitation to a dissociative potential curve along the lasers polarization axis is favored, while excitation orthogonal to the bond axis is suppressed. A similar process for ${CH_3}^0 + H^+$ dissociation is thinkable. However, hardly no dissociation curves for CH_4^+ exist, so the reason for the different structures for $CH_3^+ + H^0$ and $CH_3^+ + H^+$ dissociations remains unclear.

Dissociation into CH_2^+ can lead to two and three body fragmentation, which gives rise to several possible channels. Two body fragmentation has lower dissociation energies and is thus favored to happen (see last column in figure 3). Thus the major part of the seen events is expected to come from fragmentation into ${CH_2}^0 + H_2^+$ and $CH_2^+ + {H_2}^0$ as well as from the Coulomb explosion channel $CH_2^+ + H_2^+$. The difficulty that no coincidence measurements are possible with neutral fragments is here even stronger because count rates are lower for those processes. For a better visibility the calculated momenta for molecular hydrogen and methylene (CH_2^+) are again cut to not include the much stronger signals of H^+ and CH_3^+. The resulting distributions are shown in figure 13. For CH_2^+ the momentum distribution looks pretty similar as for CH_3^+ – the dissociation channel has very low momentum and is isotropic. A Coulomb explosion ring is hardly visible due to the other signals from CH_3^+. For H_2^+ an sharply defined isotropic spot with comparably low momentum is dominating. Beside this two other structures are visible. One highly angular dependent one with medium momentum up to 20 a.u. in longitudinal direction and

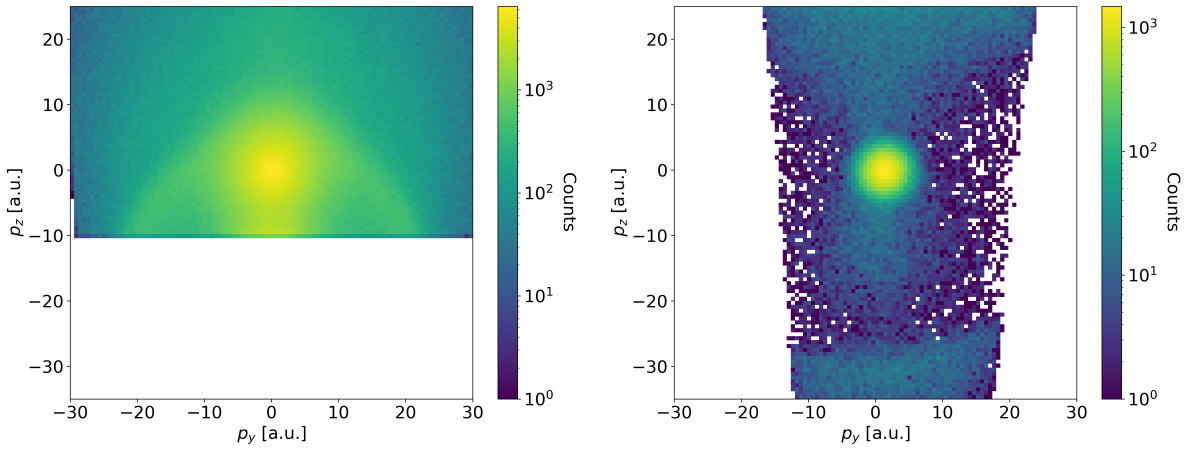

(a) momentum distribution $CH_2{}^+$

(b) momentum distribution $H_2{}^+$

Figure 13: Momentum in y-direction versus longitudinal momentum for $CH_2{}^+$ and $H_2{}^+$. The isotropic dissociation channel for $CH_2{}^+$ is seen well. The low-momentum spot of $H_2{}^+$ originates from background ionization. For $H_2{}^+$ an angle dependent structure as for H^+ is seen as well as a Coulomb explosion ring with high momentum.

a ring-like structure with high momentum of about 35 a.u.. The feature at the top originates from H^+ in a Coulomb explosion. The high momentum structure shows the Coulomb explosion into $CH_2{}^+ + H_2$. For the inner part residual hydrogen in the chamber has to be taken into account. When getting singly ionized it has no large KER corresponding to the high-intensity isotropic spot with low momentum. The angular dependent structure is therefore belonging to $CH_2{}^0 + H_2{}^+$ dissociation. This then also matches with the expected count rates for the four singly ionized dissociation pathways; the count rates decrease with rising dissociation potential. As a result, interesting similarities for the dissociation channels are observed. Both processes in which the larger fragment is ionized ($CH_3{}^+ + H^0$ and $CH_2{}^+ + H_2{}^0$) show no angular dependence and very low momenta. For the other two channels with hydrogen being ionized ($CH_3{}^0 + H^+$ and $CH_2{}^0 + H_2{}^+$), dissociation in laser direction is enhanced and the released momenta cover a larger range.

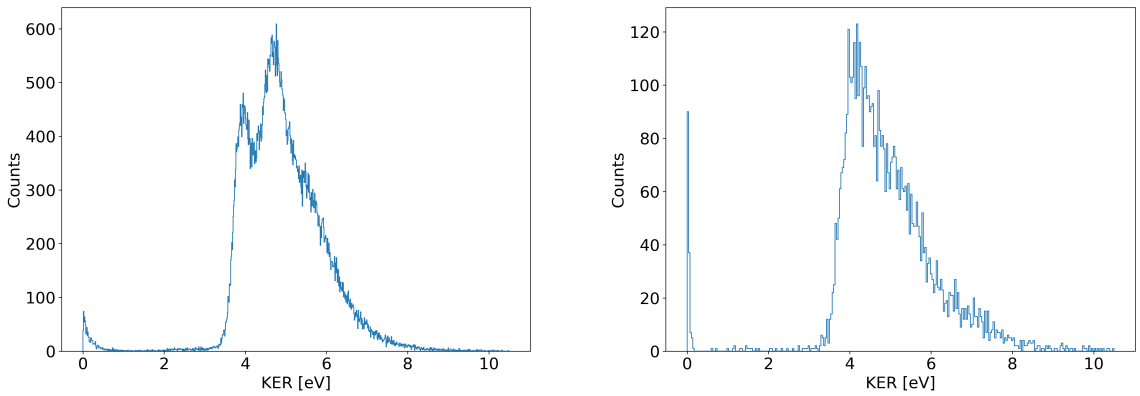

(a) $CH_3^+ + H^+$ (b) $CH_2^+ + H_2^+$

Figure 14: Kinetic energy release of Coulomb explosion channels. For $CH_3^+ + H^+$ three peaks are visible, for $CH_2^+ + H_2^+$ only one peak can be clearly identified. Both distributions show a tail like structure towards higher energies.

4.2 Single pulse Coulomb explosion

To select the Coulomb explosion channels of $CH_3^+ + H^+$ and $CH_2^+ + H_2^+$ equation 11 is used which connects the time of flight of both ions with each other. This function only depends on outer parameters as the fragments masses, the acceleration length and the applied voltage on the spectrometer. Thus it is used to extract the true coincidence events. An error of this relation is estimated by the width of the line in the two ion coincidence plot. So those events are extracted, which fulfill equation 11 within the estimated error. With this, momentum conservation in spectrometer direction (z-direction) is proven. To further rule out false coincidence events the momentum in the other two directions is calculated with equation 12. Those events for which the momenta in x and y direction are also conserved (meaning the two fragment's momenta add up to zero) are further extracted. With this process false coincidences, especially those originating from a single ionized CH_4^+ molecule together with a H^+ or H_2^+ molecule from a different ionization process, can be reduced to a minimum. From the then obtained momenta, the fragment's energy is calculated classically with $E = \frac{|\vec{p}|^2}{2m}$. The sum of the energy of both fragments is the amount of energy which was released during the dissociation. A histogram of these KER-values for both dissociation channels is shown in figure 14. The events near to zero are still from false coincidences. Both fragmentation processes show a kinetic energy distribution between 3.5 eV and 8 eV. As already seen in figure 12, this is much higher than for single ionized dissociation processes. However, thinking of a explosion driven only by Coulomb repulsion as in the $H_2^{2+} \longrightarrow H^+ + H^+$ case, the calculated energies are comparably low. The maximum energy which could be released in a $1/r$-potential at given initial bond length is much higher – taking the C–H bond length of 1.087 Å an energy of 13.2 eV is obtained.

The potential curve of CH_4^{2+} Coulomb explosion is therefore definitely not simply $1/r$ – at least not for the lowest potential curves. This was already clear because doubly ionized methane was detected as well as delayed Coulomb explosions of CH_4^{2+} in the two ion coincidence spectrum. For $CH_3^+ + H^+$ two peaks are clearly visible in the spectrum as well as a long tail-like structure towards higher energies. In this range a third peak at around 5.3 eV is identified. Fitting a triple Gaussian to this curve works quite well and gives estimates for the three observed energy peaks. The values are listed in table 1. The energy

Number	E [eV]	FWHM [eV]
(1)	3.91	0.18
(2)	4.61	0.31
(3)	5.34	0.71

Table 1: Mean energy and full width half maximum as a result of a triple-Gaussian fit towards the obtained KER spectrum for the $CH_3^+ + H^+$ Coulomb explosion process. The three peaks correspond to the visible ones in figure 14.

distance between those peaks is about 0.7 eV each. This could indicate that there are different potential curves involved in this Coulomb explosion.

Theoretical approaches for finding potential curves for the $CH_3^+ + H^+$ breakup were done by Williams et al. in 2012 [34]. They used multi-configuration self-consistent field calculations to receive possible dissociation curves. Starting from a Jahn-Teller distorted doubly ionized state of CH_4^{2+} different dissociation processes can happen. Depending on the final geometrical structure of the CH_3^+ cation, they correspond to different kinetic energy releases. Comparing the KER results with theoretical calculations shows that the measured KER spectrum is lower than possible channels predicted by theory. Other experiments measuring the KER of a Coulomb explosion into CH_3^+ and H^+ show also in general a higher energy spectrum. Experiments done with photon energies of 295 eV [34] or by collision with highly charged ions as a projectile [29] show similar structures including one or two peaks and a tail end towards higher energies. However, those spectra seem to be shifted towards higher energies by around 1 eV.

The lower energies measured in this experiment are probably due to the ionization method used. Multi-photon ionization is no instantaneous process, meaning during ionization the potential curves are modified by the laser. Thus, during the multi-photon absorption process the C−H bond length already stretches. The Coulomb explosion on the dissociation curve then starts at a larger initial bond length leading to a lower KER. A reason for the broad KER spectrum could be due to the Franck-Condon principle. The Franck-Condon region shows a regime in bond length in which the ionization can happen. This region has a certain extent leading to slightly different bond lengths for ionization and so to different KER-values. Another thing the calculated potentials in [34] indicate is the existence of metastable CH_4^{2+}. For large bond length a $\frac{1}{r}$-like potential curve is lowest in energy. For small bond lengths other potentials are lower having shallow minima and thus metastable states.

For the $CH_2^+ + H_2^+$ dissociation channel a quantitative analysis is difficult due to the much lower count rates. Optically it shows similarities to the $CH_3^+ + H^+$ spectrum. A clear peak can be identified at around 4.2 eV as well as a broad distribution towards higher energies.

Getting information about the angular distribution of direct Coulomb explosion of methane is not possible. As discussed before the detector size is too small to collect light atoms with large transversal momentum. From the momentum distribution for CH_3^+ in figure 12 it seems to be isotropic and not dependent on the lasers polarization. Since no dipole transition but only multi-photon ionization is expected to happen, this is reasonable.

4.3 Pump-probe Coulomb explosion

Pump-probe experiments can be used to investigate molecular dynamics. The first "pump" pulse plays a similar role as the pulse in the single pulse experiment. Direct Coulomb explosion is possible as well as several different single ionization pathways. After the pump pulse, the ionized molecule is not in an equilibrium position any more. This leads to rising dynamics in the molecule. Nuclear dynamics include vibrations, rotations and also dissociations as described in the theory section 2.2 for H_2. With rising intermolecular distance also ionization potentials change. Dissociation processes happen on a timescale of several hundred femtoseconds and thus can be probed by a second time-delayed pulse. With this measuring technique new break-up channels arise which are highly dependent on the time delay between both pulses. Using the three dimensional momentum resolution the ReMi provides, it is possible to get information about the intermediate dissociation curve by comparing the results to the single ionization data. For CH_4 we have observed different fragmentation channels into $CH_3{}^+ + H^0$, $CH_3{}^0 + H^+$ or $CH_2{}^+ + H_2{}^0$,$CH_2{}^0 + H_2{}^+$. The probe pulse can then further ionize the neutral fragment. In short, this can be described by a two step mechanism $CH_4 \longrightarrow CH_3{}^0 + H^+ \longrightarrow CH_3{}^+ + H^+$ as an example.

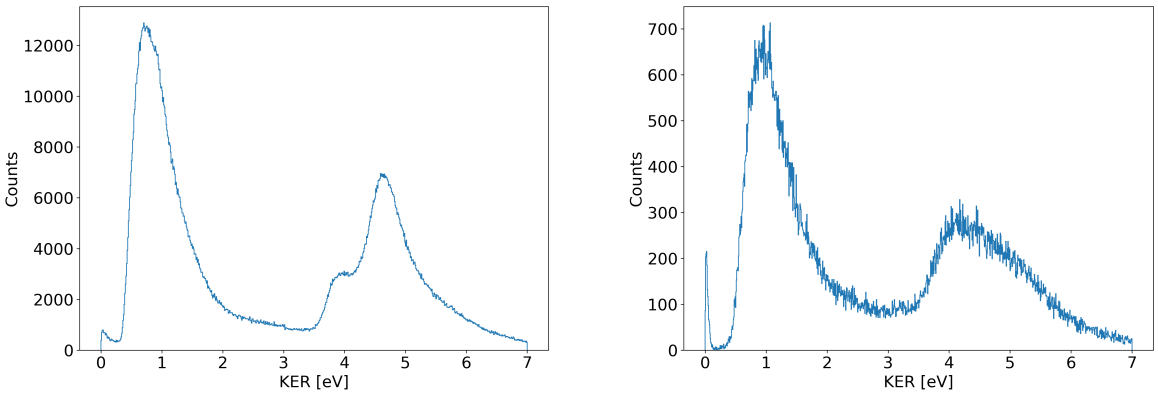

(a) $CH_3{}^+ + H^+$ (b) $CH_2{}^+ + H_2{}^+$

Figure 15: Kinetic energy release of Coulomb explosion channels in a pump-probe measurement. In comparison with the single pulse experiment a new peak appears at lower KER. This originates from a pump-probe Coulomb explosion including an intermediate state. For very short time delays this curve is higher in energy than the time-independent one.

The following analysis was done with a data set of a pump-probe measurement with methane. The delay between both pulses was varied between $-50\,\text{fs}$ and $1000\,\text{fs}$. A negative delay means the probe pulse arrives before the pump pulse. Since both pulses are identical in photon energy and intensity, no change is expected for negative time delays. The measurement was performed for longer time than the single pulse measurement analyzed before, to get higher count rates especially for the $CH_2{}^+ + H_2{}^+$ Coulomb explosion. The true coincidence events and their energies were selected and calculated as before in the single pulse coincidence measurement. The results for both Coulomb explosion channels of doubly charged methane are shown in figure 15. As in the single pulse experiment an highly energetic Coulomb explosion at around $4\,\text{eV}$ is observed. However, its structure is not visible that clearly as in the single pulse case, but still good enough to distinguish two peaks at $3.9\,\text{eV}$ and $4.6\,\text{eV}$ for $CH_3{}^+ + H^+$. Related to the single pulse Coulomb explosion, here only one of the two pulses directly double ionizes the methane molecule followed by a Coulomb explosion. The second pulse has no further influence. More interesting

is the appearance of a second peak at much lower energy which is in fact the dominating process for both fragmentations into $CH_3^+ + H^+$ and $CH_2^+ + H_2^+$. This could be as in the H_2 case explained in chapter 2.2 due to a two step Coulomb explosion. The pump pulse singly ionizes the molecule, while after some time delay the probe pulse removes a second electron leading to a methane dication which dissociates. This process should then be dependent on the time delay between both pulses. Therefore in the next step the time delay dependence of the KER is analyzed for both fragmentation channels $CH_3^+ + H^+$ and $CH_2^+ + H_2^+$ individually.

4.3.1 $CH_3^+ + H^+$ Coulomb explosion

To be able to see this time dependence the obtained kinetic energies are plotted as a function of the varied time delay. The time evolution of the KER distribution can be seen in figure 16. Clearly two different curve types can be distinguished. The direct Coulomb explosion process shows the same KER value independent of time delay. This strengthens the idea that for this double ionization only one pulse is involved. In contrast, the second channel appearing in the pump-probe measurement is highly dependent on the time delay. For very short time delays smaller than 20 fs the time dependent dissociation channel has even a larger KER than the time independent one. With a full width at half maximum of 12 fs of one single pulse this means that for such short time delays the pulses are largely overlapping with each other. At some point making a difference between both pulses is not possible any more which in fact means the pulses merge to one longer one with higher intensity. So for the Coulomb explosion with one pulse it has to be taken into account that a two step mechanism is also possible within the time duration of a single pulse. Potentially, this could explain the highly energetic tail structure seen in the single pulse experiment. Towards longer time delays the KER of the time-dependent Coulomb explosion is getting smaller though still a finite KER value remains. Interestingly for those intermediate to long time delays the KER distribution of the time dependent process has a sharp edge towards small energies but a broad distribution towards higher energies.

In the next step the intensities for different time delays are compared. This cannot simply be done out of the figure above, because not for every time delay an equivalent amount of measurements was taken. A correction for this is necessary. That is why the H_2O^+ signal is used as a reference. Because the ionization of water happens in one step, the yield rate should be in theory independent of time delay. Deviations from this are thus due to a different number of measurements taken. Therefore the spectrum in figure 16 is normalized with the time-delay dependent number of water ionization events. The result is shown in figure 17 (the red curve is ignored for this moment). This is still not perfect, because large transversal momenta of H^+ cannot be detected which could lead to a decrease in count rate for rising KER-values. For the time dependent Coulomb explosion highest intensities are reached at time delays of about 400 fs. The time independent Coulomb explosion signal at 4.6 eV is strongly reduced in intensity with longer time delay. For a time delay of about 1000 fs both direct Coulomb explosion peaks are again clearly separated and have similar count rates, like in the single pulse measurement.

For H_2 pump-probe Coulomb explosion it is supposed that the intermediate H_2^+ ion is travelling along a dissociation curve before being ionized a second time to a purely Coulomb repulsive potential curve. Assuming this process to happen here as well, the total KER is depending on two dissociation curves. For the Coulomb explosion curve $CH_4^{2+} \longrightarrow CH_3^+ + H^+$ a first assumption is a simple $1/r$ Coulomb repulsion potential. Then the question arises at which internuclear C–H distance r_M the second ionization takes place. $r_M(t_d)$ has to be a function of time delay t_d, even though the exact functional dependence

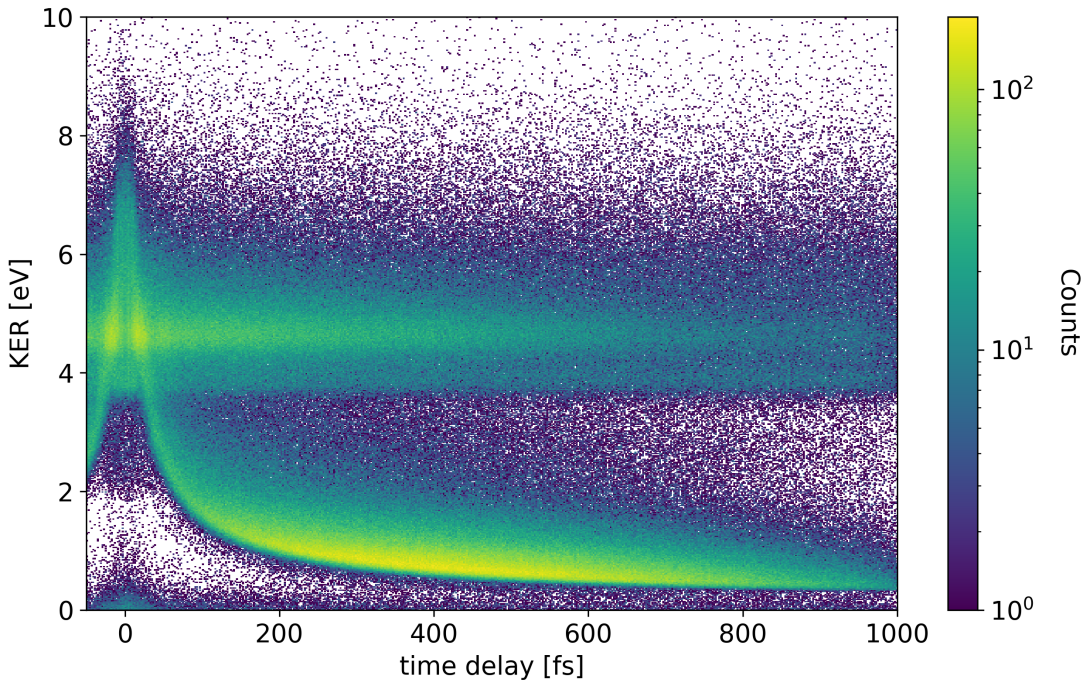

Figure 16: KER of $CH_3{}^+ + H^+$ as a function of time. A time dependent channel as well as the time independent one can be seen.

is unknown, because the shape of the intermediate potential curve is not known either. Therefore the simplest approach is to use a constant velocity v with which the two fragments are instantaneously moving apart from each other after the first ionization took place. This is of course not realistic, but showed good results for other pump-probe Coulomb explosion experiments with similar molecules [2]. For the radius of the second ionization this means $r_M = r_0 + vt_d$ where r_0 describes the initial distance between the hydrogen atom and the other atoms in the CH_4 ground state. This is roughly assessed with the bond length CH_3–H between one hydrogen atom and the center of mass of the remaining four atoms. Additionally, the kinetic energy release during the dissociation on the intermediate potential curve has to be added; in the simplest model this is assumed to be constant, independent of how long the time delay is. To get a rough estimate of the quality of these assumptions three curves were fitted with different parameters used as variables:

1. $\mathrm{KER}(t_d) = \frac{q^2}{4\pi\epsilon_0}\frac{1}{r_0+vt_d} + C$ (r_0,v,C as variables)
2. $\mathrm{KER}(t_d) = \frac{q^2}{4\pi\epsilon_0}\frac{1}{r_0+vt_d} + C$ (v,C as variables, $r_0 = 1.185\,\text{Å}$)
3. $\mathrm{KER}(t_d) = \frac{q^2}{4\pi\epsilon_0}\frac{1}{r_0+vt_d} + \frac{\mu}{2}v^2$ (v as a variable, $r_0 = 1.185\,\text{Å}$)

In the last function the kinetic energy gain due to the travelling on the intermediate dissociation curve was estimated with the classical kinetic energy $\frac{\mu}{2}v^2$ of two bodies moving apart from each other with a constant velocity v. μ is the reduced mass of the two final fragments. The best fit of function 3 was used in figure 17 as an example of the quality of the fit function.

In general all three functions are in good agreement with the actual curve. The obtained parameters are

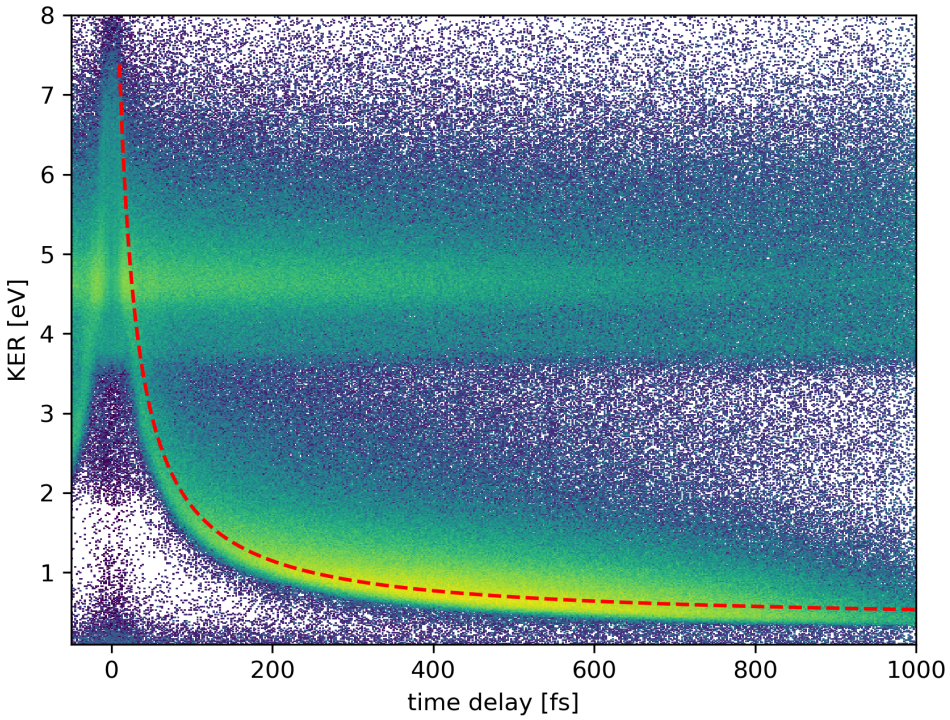

Figure 17: KER of $CH_3{}^+ + H^+$ as a function of time with normalized yield rates. A logarithmic color map is used. The red curve shows the fit of a $\frac{1}{r}$ potential curve modified with an initial KER due to the intermediate step.

Fit	v [$\frac{m}{s}$]	r_0 [Å]	C [eV]
1	8470 ± 120	1.68 ± 0.05	0.305 ± 0.005
2	9510 ± 60	1.185[1]	0.339 ± 0.004
3	8700 ± 80	1.185[1]	0.370 ± 0.005[2]

Table 2: Obtained parameters for different fit functions. Shown errors are only errors originating from the fitting process.
[1] Fixed value of initial center of mass distance between H and CH_3.
[2] Value and error calculated from obtained velocity.

shown in table 2. They differ to some extent but are all in the same region showing that the function is not highly sensitive towards changes of bond length and dissociation velocity. Specifically, the taken approximation of the initial velocity and the behavior on the intermediate dissociation curve does not show problems. Since hardly no theory exists for $CH_4{}^+$ dissociation, a further quantitative analysis is not possible. At least, the assumed $\frac{1}{r}$ potential for the Coulomb explosion curve is in good agreement with the results. Theory predicts a $\frac{1}{r}$ like potential curve for larger internuclear distances to be lowest in energy for $CH_4{}^{2+} \longrightarrow CH_3{}^+ + H^+$ dissociation as well [34].

Angular structure

For dissociation of $CH_4{}^+$ in a single-pulse experiment, the observed channels showed completely different angular distributions of the ion's momenta. While the $CH_3{}^+ + H^0$ channel has an isotropic momentum distribution, the break-up into $CH_3{}^0 + H^+$ is only possible along the laser's polarization axis. In the previous section it was discussed that the time dependent Coulomb explosion is likely to have an intermediate singly ionized dissociative state. Therefore the angular distribution of this time delayed Coulomb explosion gets interesting. This is done for different time delays ranging from 50 fs to 950 fs. Smaller time delays are not possible to include since then the events are overlapping with the direct Coulomb explosion. So the spectrum was sliced into 6 regions each containing a time delay range of 150 fs. For each range the y-momentum is plotted against the longitudinal one as showed in figure 19. The momentum distribution of the H^+ fragment is used, but due to momentum conservation there is no structural difference to the one of $CH_3{}^+$.

The total momentum gets smaller with increasing time delay as a consequence of the decreasing KER. The distribution is clearly angle-dependent as Coulomb explosions along the laser polarization axis are much higher in intensity. However, a circular shape of distribution is still observable, in contrast to the $CH_3{}^0 + H^+$ dissociation where almost no events were detected in the horizontal plane. In the amount of released momentum the two channels of $CH_3{}^0 + H^+$ and $CH_3{}^+ + H^+$ show similarities especially for large time delays. This could indicate that pump-probe Coulomb explosion happens from ionizing the neutral CH_3 fragment during the dissociation. But also this idea has problems; so it is not explained why for $CH_3{}^0 + H^+$ dissociation KERs from 0 eV to 0.8 eV are almost equally distributed, while for the Coulomb explosion channel one specific KER is most likely.

For small time delays fragments show too large momenta so again not the full spectrum can be resolved. To get an idea if the angular distribution changes with time delay is therefore hardly possible. At least for large time delays the angular distribution of the $CH_3{}^+ + H^+$ can be compared with the dissociation into $CH_3{}^0 + H^+$. This is done in figure 18, where the count rate for different angles in respect to the laser polarization axis ϑ is plotted. For both plots only an energy range below 0.85 eV was selected, such that the detector shows no limitations for hydrogen ions. However, just calculating and plotting the angle

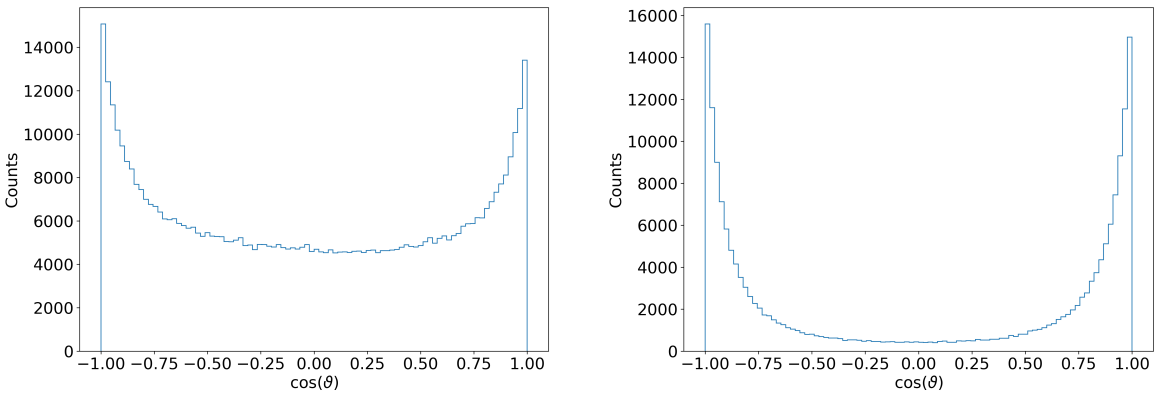

(a) $CH_3{}^+ + H^+$ (b) $CH_3{}^0 + H^+$

Figure 18: Angular dependence of time delayed Coulomb explosion with KER $< 0.85\,\text{eV}$. ϑ is the angle between the hydrogen fragment and the laser polarization axis. The cosine is used to normalize the distribution.

would lead to a biased distribution since an angle of 90° has a much higher probability than one of 0°. To correct for this the cosine of the angle is plotted. If the dissociation is parallel to the laser polarization axis, the angle is 0° corresponding to $\cos\vartheta = \pm 1$. Dissociation in the horizontal plane therefore means $\cos\vartheta = 0$. As seen before both channels are angular dependent but show differences in their strength, because for pump-probe Coulomb explosion dissociation in the horizontal plane is still possible.

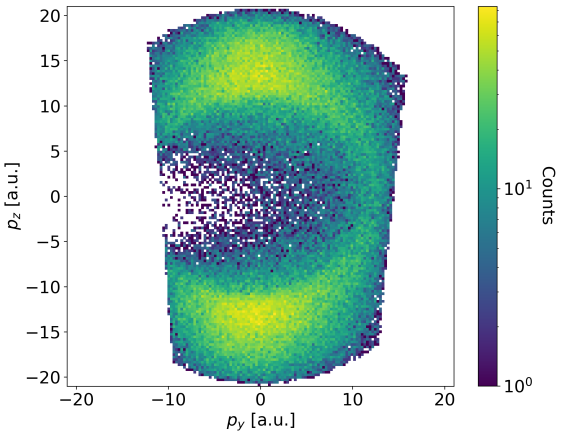

(a) 50 fs $< t_{delay} <$ 200 fs

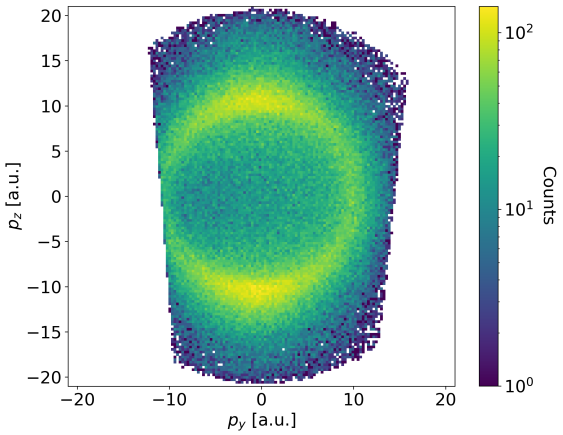

(b) 200 fs $< t_{delay} <$ 350 fs

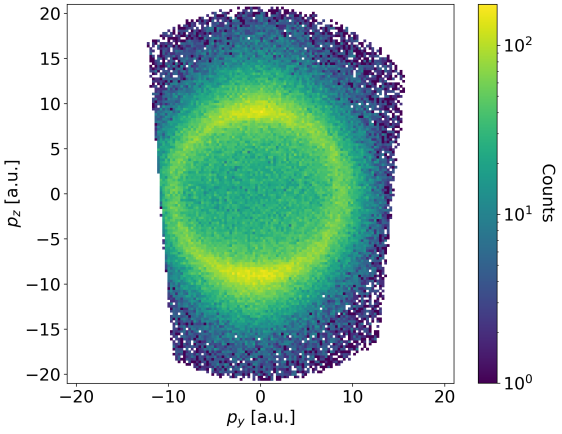

(c) 350 fs $< t_{delay} <$ 500 fs

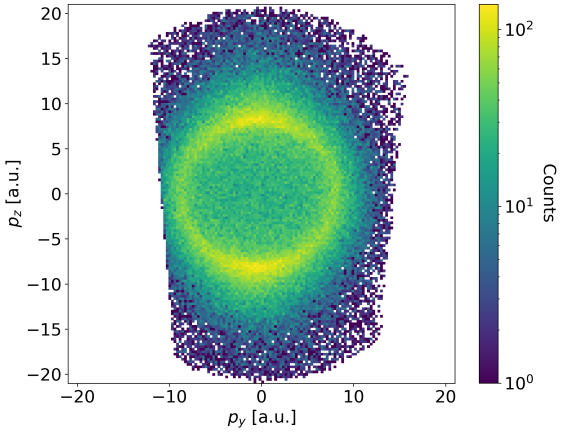

(d) 500 fs $< t_{delay} <$ 650 fs

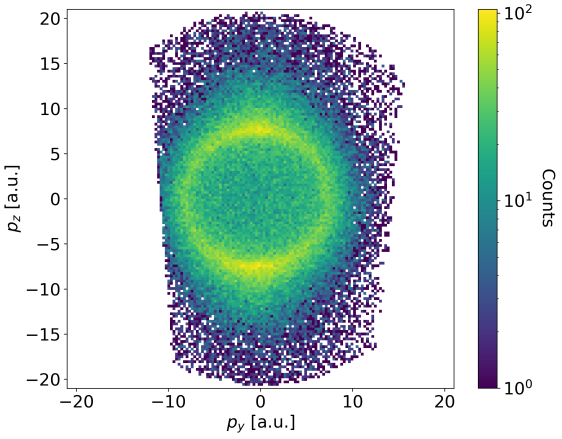

(e) 650 fs $< t_{delay} <$ 800 fs

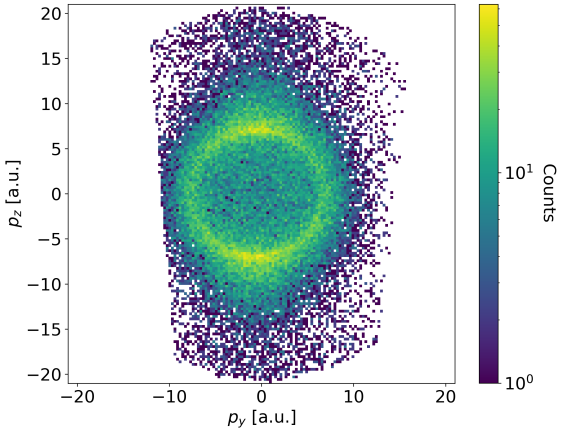

(f) 800 fs $< t_{delay} <$ 950 fs

Figure 19: Momentum in y-direction versus longitudinal momentum of H^+ for time delayed Coulomb explosion of ${CH_3}^+ + H^+$.

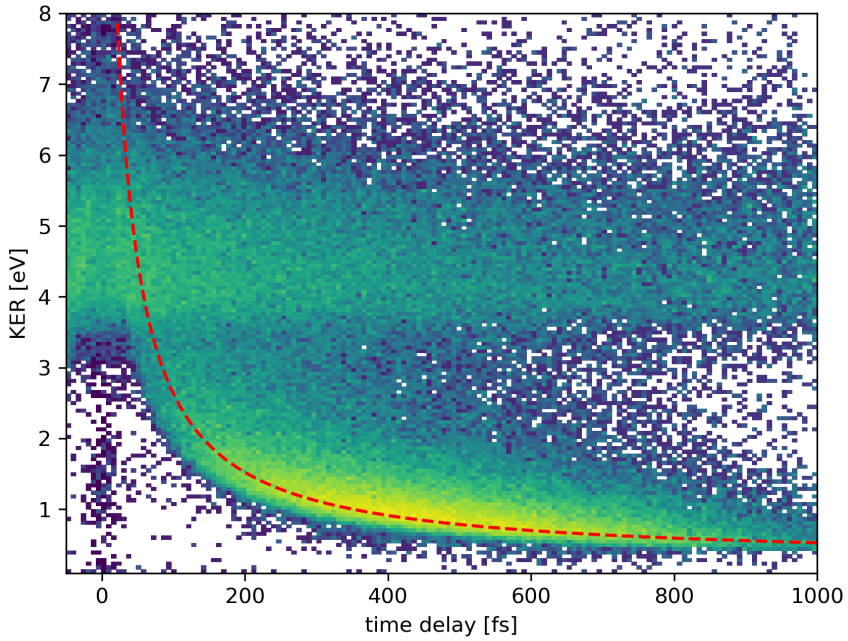

Figure 20: KER of $CH_2^+ + H_2^+$ Coulomb explosion as a function of time delay with normalized yield rates. A logarithmic color map is used. As for $CH_3^+ + H^+$ a time dependent and a time independent channel is seen. The red curve shows the fit of a $\frac{1}{r}$ potential curve modified with an initial KER due to an intermediate step in a pump-probe Coulomb explosion.

4.3.2 $CH_2^+ + H_2^+$ Coulomb explosion

In the single pulse experiment breakups into $CH_3 + H$ and $CH_2 + H_2$, with one of the two or both fragments being ionized, were detected. Comparing them with each other, it was observed that both dissociation channels each as well as the Coulomb explosion channels show large commonalities in energy and momentum distribution. In this part the time dependent features for Coulomb explosions into CH_2^+ and H_2^+ are investigated in the same way as for $CH_3^+ + H^+$. Figure 20 shows the already intensity corrected KER plot as a function of time delay – together with a fit function for the time dependent channel. The behavior of the Coulomb explosion is similar to that of $CH_3^+ + H^+$ – a time independent as well as a time dependent channel is seen. Count rates are much lower for $CH_2^+ + H_2^+$. It was already the case for CH_4^+ dissociations, that dissociation energies were higher when molecular hydrogen is produced, so it is not surprising that this holds on for the CH_4^{2+} Coulomb explosion as well. The intensity decrease of the direct Coulomb explosion channel with rising time delay is quite significant even after the two 12 fs long pulses do not overlap with each other any more. For the time dependent curve, intensity is again highest at around 400 fs. The feature at very small time delays, that the time dependent dissociation curve is elongated and shows higher energies than the time independent Coulomb explosion, is much weaker. In fact, it is not clearly resolvable because also for the direct Coulomb explosion channel higher energies continuously shrink with rising time delay. So it is hard to say to what extent there are different processes at time scales where both pulses overlap with each other.

In order to quantify the pump-probe Coulomb explosion process, a $\frac{1}{r}$ potential is assumed and the same three functions as in 4.3.1 are fitted along the curve. For the initial bond length the CH_2–H_2 equilibrium

Fit	v [$\frac{m}{s}$]	r_0 [Å]	C [eV]
1	5250 ± 350	1.02 ± 0.39	0.306 ± 0.026
2	5510 ± 100	0.717^1	0.323 ± 0.013
3	5360 ± 100	0.717^1	0.262 ± 0.007^2

Table 3: Obtained parameters for different fit functions. Shown errors are only errors originating from the fitting process.
[1] Fixed value of initial center of mass distance between H_2 and CH_2.
[2] Value and error calculated from obtained velocity.

distance of 0.717 Å was used; the results are shown in table 3. Again the given errors are only coming from the fit and are thus not meaningful. The fitting procedure leads to good results as figure 20 shows. For this plot, curve 3 using only the velocity as a free fit parameter was taken. Noticeable is the much lower calculated dissociation velocity compared to $CH_3{}^+ + H^+$ Coulomb explosion. This corresponds to the seen effect that the KER decreases much slower with rising time delay, which was also observed by other pump-probe experiments with methane [21].

All together this leads to a conclusion that Coulomb explosion processes of $CH_3{}^+ + H^+$ and $CH_2{}^+ + H_2{}^+$ are remarkable similar in structure. A $\frac{1}{r}$ potential seems to be a good approximation for the $CH_2{}^+ + H_2{}^+$ Coulomb explosion as well. The slower shrinking KER for the pump-probe Coulomb explosion could be caused by a shallower potential curve of the intermediate dissociative state of $CH_4{}^+$.

Lastly, the angular distribution of the fragments momenta is considered for different time delays. For a better comparison the same 6 time intervals ranging from 50 fs to 950 fs are used to plot the momentum in y-direction against the longitudinal momentum. The resulting figures are shown in 21. Again, similarities to the $CH_3{}^+ + H^+$ Coulomb explosion are clearly visible. The laser polarization axis is favored for Coulomb explosion although events can be observed for every direction.

Now, the question arises again which intermediate state was taken during the time dependent Coulomb explosion. The momenta being significantly apart from zero even for long time delays mismatch with the low released momenta in $CH_2{}^+ + H^0$ dissociation. The angular dependent explosion process supports the idea that time-delayed Coulomb explosion primarily happens by ionizing the neutral methylene component in $CH_2{}^0 + H^+$ dissociation.

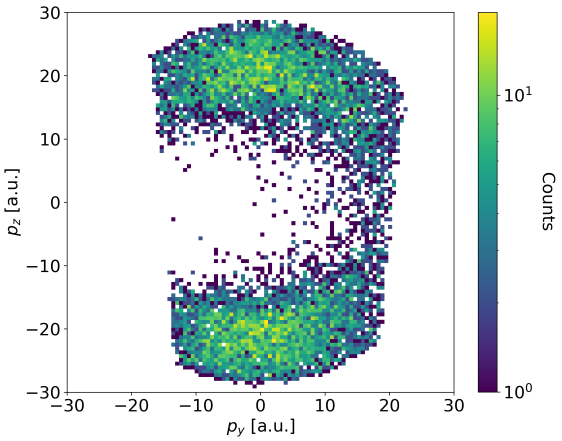

(a) 50 fs $< t_{delay} <$ 200 fs

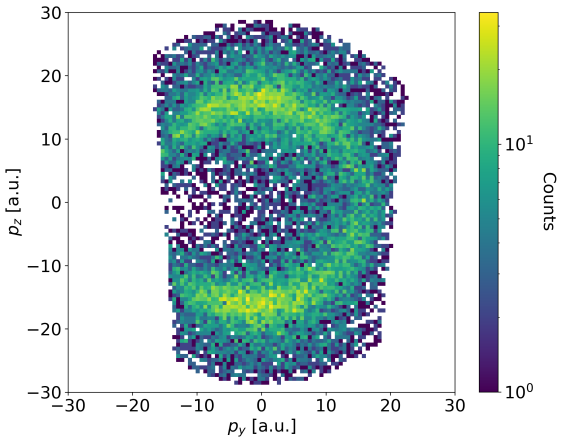

(b) 200 fs $< t_{delay} <$ 350 fs

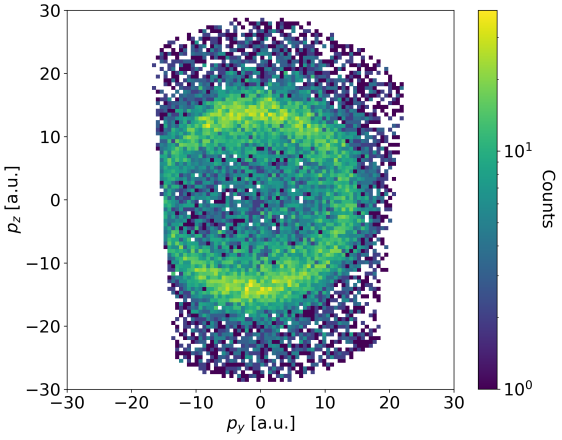

(c) 350 fs $< t_{delay} <$ 500 fs

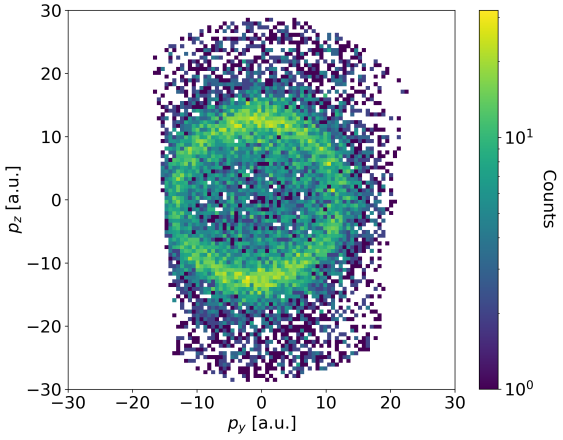

(d) 500 fs $< t_{delay} <$ 650 fs

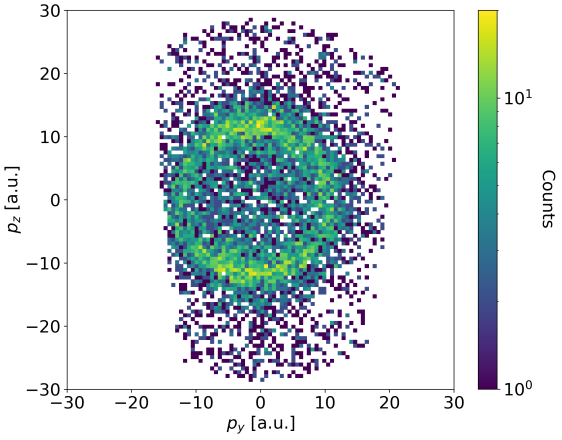

(e) 650 fs $< t_{delay} <$ 800 fs

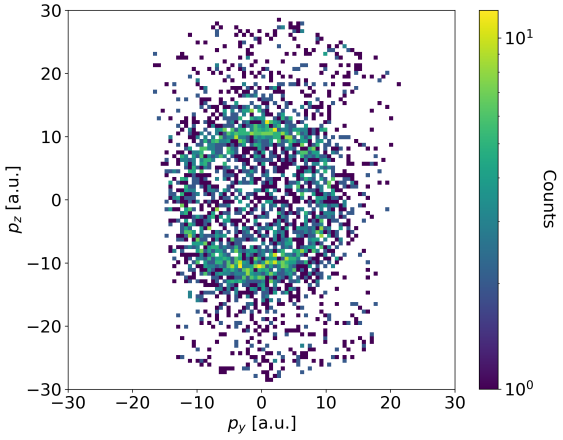

(f) 800 fs $< t_{delay} <$ 950 fs

Figure 21: Momentum in y-direction versus longitudinal momentum of H^+ for time delayed Coulomb explosion of $CH_2{}^+ + H_2{}^+$.

5 Conclusion and Outlook

This work covered the analysis of two-body fragmentation channels of methane with a pulsed laser in a Reaction Microscope. Two experiments were considered, one single pulse and a pump-probe experiment with varying time delay. Dissociations and Coulomb explosions into $CH_3^+ + H^+$ and $CH_2^+ + H_2^+$ were observed and compared. Since fragments are measured in coincidence, different reaction channels can be selected for further analysis. The ReMi enables a three dimensional momentum reconstruction. This was used to calculate the kinetic energy release as well as the angular distribution of the different dissociation processes.

Large similarities have been observed for the four fragmentation channels of singly ionized methane. Dissociations after single ionization of methane were analyzed in a single pulse measurement. As expected, the count rates of the different fragmentations correspond to the order of the dissociation potentials. So the fragmentations into $CH_3^+ + H^0$ and $CH_2^+ + H^0$ are much more likely than the ones into $CH_3^0 + H^+$ and $CH_2^0 + H_2^+$. The angular distribution of the channels showed structural differences depending on which fragment is ionized. While $CH_3^+ + H^0$ and $CH_2^+ + H^0$ show no dependence on the orientation of the fragments towards the laser polarization axis, for $CH_3^0 + H^+$ and $CH_2^0 + H_2^+$ dissociations it is highly favored that the molecule dissociates parallel to the laser polarization. This could indicate a dipole transition in the dissociation process which suppresses dissociation perpendicular to the laser polarization.

Also Coulomb explosions into $CH_3^+ + H^+$ and $CH_2^+ + H_2^+$ were observed in the single pulse experiment originating from double ionized methane. The KER of those processes was peaked at around 4 eV to 5 eV each. This is much higher than for other dissociations channels, but strongly below a $\frac{1}{r}$ potential curve. This means for small internuclear distances other potential curves are energetically lower which is in agreement with observed CH_4^{2+} on the detector and theoretical calculations [34].

In a pump-probe experiment a second – time dependent – Coulomb explosion channel could be observed. This can be explained by a similar mechanism as for H_2 that the first pulse leads to single ionization which is then followed by a dissociation of the molecule [26]. During this dissociation the second pulse further ionizes the neutral fragment leading to a Coulomb explosion process. For the released kinetic energy is was shown that this Coulomb explosion curve follows a $\frac{1}{r}$ potential with an initial kinetic energy originating from the dissociation process. This structure is very similar for both $CH_3^+ + H^+$ and $CH_2^+ + H_2^+$ channels. Using the angular distribution of the time dependent Coulomb explosion can help to identify the intermediate dissociation curve. It is clearly observable that the Coulomb explosion is most probable in spectrometer direction. For longer time delays a comparison of the angular distribution for $CH_3^0 + H^+$ and $CH_3^+ + H^+$ could be done showing similar structures. The main difference is that dissociations perpendicular to the laser polarization are not completely impossible for $CH_3^+ + H^+$. Nevertheless, it seems to be likely that the $CH_3^0 + H^+$ and $CH_2^0 + H_2^+$ dissociation channels play some role as an intermediate state in pump-probe Coulomb explosion.

For many cases problems arose due to small detector size so that not all ions could be detected. For example, it would be of interest if the angular distribution of the time dependent Coulomb explosion shows changes for small time delays. A method to reduce this problem is using higher spectrometer voltages or change the polarization direction of the laser in regard to the spectrometer axis. Both methods were done in recent experiments.

Further analysis could also focus on a three body Coulomb explosion process into $CH_2^+ + H^+ + H^+$ in

order to compare this to the two body fragmentation processes analyzed in this work. Another possibility could be to further include the photoelectrons emitted in the dissociation and Coulomb explosion process.

A Atomic units (a.u.)

In atomic physics typical length scales, masses and energies are very small. Thus the use of atomic units is very convenient, a dimensionless system of units using properties typical to the hydrogen atom. Four physical constants are dedicated to the value of 1: the electrons mass m_e and charge q_e, the reduced Planck constant $\hbar$ and the Coulomb constant $\frac{1}{4\pi\epsilon_0}$. In table 4 basic quantities and their respective SI-value are listed.

quantity	unit	value in SI units
mass	m_e electron rest mass	$1.661 \times 10^{-31}\,\mathrm{kg}$
charge	q_e elementary charge	$1.602 \times 10^{-19}\,\mathrm{C}$
angular momentum	$\hbar$ reduced Planck constant	$1.055 \times 10^{-34}\,\mathrm{J\,s}$
length	a_B Bohr radius	$5.292 \times 10^{-11}\,\mathrm{m}$
velocity	$v_0 = \alpha c_0$	$2.188 \times 10^{6}\,\mathrm{m\,s^{-1}}$
momentum	$p_0 = m_e v_0$	$1.993 \times 10^{-24}\,\mathrm{kg\,m\,s^{-1}}$
energy	$E_h = 2R_y = \alpha^2 m_e c_0^2$ Hartree Energy	$4.360 \times 10^{-18}\,\mathrm{J} = 27.21\,\mathrm{eV}$
time	$t = \hbar E_h^{-1}$	$2.419 \times 10^{-17}\,\mathrm{s}$

Table 4: Physical quantities in atomic units and their corresponding SI-value. $\alpha = \frac{1}{137}$ is the fine structure constant, $R_y = 13.6\,\mathrm{eV}$ the Rydberg energy.

References

[1] P. Agostini et al. "Free-Free Transitions Following Six-Photon Ionization of Xenon Atoms." In: *Phys. Rev. Lett.* 42 (17 Apr. 1979), pp. 1127–1130. DOI: 10.1103/PhysRevLett.42.1127. URL: https://link.aps.org/doi/10.1103/PhysRevLett.42.1127.

[2] Felix Allum et al. "Coulomb explosion imaging of CH3I and CH2ClI photodissociation dynamics." In: *The Journal of Chemical Physics* 149.20 (Nov. 2018), p. 204313. ISSN: 0021-9606. DOI: 10.1063/1.5041381. eprint: https://pubs.aip.org/aip/jcp/article-pdf/doi/10.1063/1.5041381/15552547/204313_1_online.pdf. URL: https://doi.org/10.1063/1.5041381.

[3] M. V. Ammosov, N. B. Delone, and V. P. Krainov. "Tunnel ionization of complex atoms and of atomic ions in an alternating electromagnetic field." In: *Soviet Journal of Experimental and Theoretical Physics* 64.6 (Dec. 1986), p. 1191.

[4] T. Ast et al. "Doubly charged molecular ions of methane." In: *Chemical Physics Letters* 78.3 (1981), pp. 439–441. ISSN: 0009-2614. DOI: https://doi.org/10.1016/0009-2614(81)85232-3. URL: https://www.sciencedirect.com/science/article/pii/0009261481852323.

[5] M. Born and R. Oppenheimer. "Zur Quantentheorie der Molekeln." In: *Annalen der Physik* 389.20 (1927), pp. 457–484. DOI: https://doi.org/10.1002/andp.19273892002. eprint: https://onlinelibrary.wiley.com/doi/pdf/10.1002/andp.19273892002. URL: https://onlinelibrary.wiley.com/doi/abs/10.1002/andp.19273892002.

[6] Merrick J. DeWitt and Robert J. Levis. "Calculating the Keldysh adiabaticity parameter for atomic, diatomic, and polyatomic molecules." In: *The Journal of Chemical Physics* 108.18 (May 1998), pp. 7739–7742. ISSN: 0021-9606. DOI: 10.1063/1.476208. eprint: https://pubs.aip.org/aip/jcp/article-pdf/108/18/7739/10790622/7739_1_online.pdf. URL: https://doi.org/10.1063/1.476208.

[7] A. Einstein. "Über einen die Erzeugung und Verwandlung des Lichtes betreffenden heuristischen Gesichtspunkt." In: *Annalen der Physik* 322.6 (1905), pp. 132–148. DOI: https://doi.org/10.1002/andp.19053220607. eprint: https://onlinelibrary.wiley.com/doi/pdf/10.1002/andp.19053220607. URL: https://onlinelibrary.wiley.com/doi/abs/10.1002/andp.19053220607.

[8] Professor E. Rutherford F.R.S. "LXXIX. The scattering of α and β particles by matter and the structure of the atom." In: *The London, Edinburgh, and Dublin Philosophical Magazine and Journal of Science* 21.125 (1911), pp. 669–688. DOI: 10.1080/14786440508637080. eprint: https://doi.org/10.1080/14786440508637080. URL: https://doi.org/10.1080/14786440508637080.

[9] Lutz Fechner. "High resolution experiments on strong-field ionization of atoms and molecules: test of tunneling theory, the role of doubly excited states, and channel-selective electron spectra." PhD thesis. Ruprecht-Karls-Universität Heidelberg, 2014.

[10] R Flammini et al. "The role of the methyl ion in the fragmentation of CH42+." In: *New Journal of Physics* 11.8 (Aug. 2009), p. 083006. DOI: 10.1088/1367-2630/11/8/083006. URL: https://dx.doi.org/10.1088/1367-2630/11/8/083006.

[11] Patrick Froß. "Electron-nuclear correlation, singly-excited Rydberg states and electron emission asymmetry in multiphoton ionization of H2." PhD thesis. Ruprecht-Karls-Universität Heidelberg, 2020.

[12] Kenji Furuya et al. "Dissociation dynamics of CH+4 core ion in the 2A1 state." In: *The Journal of Chemical Physics* 101.4 (Aug. 1994), pp. 2720–2728. ISSN: 0021-9606. DOI: 10.1063/1.467653. eprint: https://pubs.aip.org/aip/jcp/article-pdf/101/4/2720/10773739/2720_1_online.pdf. URL: https://doi.org/10.1063/1.467653.

[13] Albert Gold and H. Barry Bebb. "Theory of Multiphoton Ionization." In: *Phys. Rev. Lett.* 14 (3 Jan. 1965), pp. 60–63. DOI: 10.1103/PhysRevLett.14.60. URL: https://link.aps.org/doi/10.1103/PhysRevLett.14.60.

[14] H. Hertz. *Ueber einen Einfluss des ultravioletten Lichtes auf die electrische Entladung*. Jan. 1887. DOI: 10.1002/andp.18872670827. URL: https://doi.org/10.1002/andp.18872670827.

[15] Eizi Hirota. "Anharmonic potential function and equilibrium structure of methane." In: *Journal of Molecular Spectroscopy* 77.2 (1979), pp. 213–221. ISSN: 0022-2852. DOI: https://doi.org/10.1016/0022-2852(79)90103-6. URL: https://www.sciencedirect.com/science/article/pii/0022285279901036.

[16] C. P. Schulz I. V. Hertel. *Atoms, Molecules and Optical Physics 1*. Springer, 2015. DOI: 10.1007/978-3-642-54322-7. URL: https://doi.org/10.1007/978-3-642-54322-7.

[17] C. P. Schulz I. V. Hertel. *Atoms, Molecules and Optical Physics 2*. Springer, 2015. DOI: 10.1007/978-3-642-54313-5. URL: https://doi.org/10.1007/978-3-642-54313-5.

[18] H. A. Jahn and E. Teller. "Stability of polyatomic molecules in degenerate electronic states - I—Orbital degeneracy." In: *Proc. R. Soc. Lond. A* 161 (1937), pp. 220–235. DOI: 10.1098/rspa.1937.0142. URL: http://doi.org/10.1098/rspa.1937.0142.

[19] Hiroyuki Katsuki et al. "Visualizing Picometric Quantum Ripples of Ultrafast Wave-Packet Interference." In: *Science* 311.5767 (2006), pp. 1589–1592. ISSN: 00368075, 10959203. URL: http://www.jstor.org/stable/3845665 (visited on 08/20/2023).

[20] L. V. Keldysh. "Ionization in the field of a strong electromagnetic wave." In: *Soviet Journal of Experimental and Theoretical Physics* 20.5 (1965), pp. 1307–1314.

[21] Min Li et al. "Ultrafast imaging of spontaneous symmetry breaking in a photoionized molecular system." In: *Nature Communications* 12.4233 (July 2021). ISSN: 2041-1723. DOI: 10.1038/s41467-021-24309-z. URL: https://doi.org/10.1038/s41467-021-24309-z.

[22] I. V. Litvinyuk et al. "Alignment-Dependent Strong Field Ionization of Molecules." In: *Phys. Rev. Lett.* 90 (23 June 2003), p. 233003. DOI: 10.1103/PhysRevLett.90.233003. URL: https://link.aps.org/doi/10.1103/PhysRevLett.90.233003.

[23] T. H. Maiman. "Stimulated Optical Radiation in Ruby." In: *Nature* 187.4736 (1960), pp. 493–494. DOI: 10.1038/187493a0. URL: https://doi.org/10.1038/187493a0.

[24] *SLM-S640 USB/Ethernet SLM-S320 USB/Ethernet – Technical documentation and instructions for use.*

[25] R. Moshammer et al. "Low-Energy Electrons and Their Dynamical Correlation with Recoil Ions for Single Ionization of Helium by Fast, Heavy-Ion Impact." In: *Phys. Rev. Lett.* 73 (25 Dec. 1994), pp. 3371–3374. DOI: 10.1103/PhysRevLett.73.3371. URL: https://link.aps.org/doi/10.1103/PhysRevLett.73.3371.

[26] Peng Peng et al. "Intensity-dependent study of strong-field Coulomb explosion of H2." In: *Opt. Express* 23.14 (July 2015), pp. 18763–18768. DOI: 10.1364/OE.23.018763. URL: https://opg.optica.org/oe/abstract.cfm?URI=oe-23-14-18763.

[27] N. Bohr Dr. phil. "I. On the constitution of atoms and molecules." In: *The London, Edinburgh, and Dublin Philosophical Magazine and Journal of Science* 26.151 (1913), pp. 1–25. DOI: 10.1080/14786441308634955. eprint: https://doi.org/10.1080/14786441308634955. URL: https://doi.org/10.1080/14786441308634955.

[28] J W Rabalais et al. "The Jahn-Teller Effect in the Electron Spectrum of Methane." In: *Physica Scripta* 3.1 (Jan. 1971), p. 13. DOI: 10.1088/0031-8949/3/1/004. URL: https://dx.doi.org/10.1088/0031-8949/3/1/004.

[29] Jyoti Rajput et al. "Unexplained dissociation pathways of two-body fragmentation of methane dication." In: *The Journal of Chemical Physics* 156.5 (Feb. 2022), p. 054301. ISSN: 0021-9606. DOI: 10.1063/5.0079851. eprint: https://pubs.aip.org/aip/jcp/article-pdf/doi/10.1063/5.0079851/16769844/054301_1_online.pdf. URL: https://doi.org/10.1063/5.0079851.

[30] T. Severt et al. "Two-body dissociation of formic acid following double ionization by ultrafast laser pulses." In: *Phys. Rev. A* 105 (5 May 2022), p. 053112. DOI: 10.1103/PhysRevA.105.053112. URL: https://link.aps.org/doi/10.1103/PhysRevA.105.053112.

[31] A. Sommerfeld. "Zur Quantentheorie der Spektrallinien." In: *Annalen der Physik* 356.17 (1916), pp. 1–94. DOI: https://doi.org/10.1002/andp.19163561702. eprint: https://onlinelibrary.wiley.com/doi/pdf/10.1002/andp.19163561702. URL: https://onlinelibrary.wiley.com/doi/abs/10.1002/andp.19163561702.

[32] Florian Trost. "Time-resolved Fragmentation of Diiodomethane studied in an XUV Pump-Probe Experiment." PhD thesis. Ruprecht-Karls-Universität Heidelberg, 2023.

[33] Feng Wang. "Molecular orbitals of methane: symmetry or hybridization?" In: *Journal of Molecular Structure: THEOCHEM* 678.1 (2004), pp. 105–111. ISSN: 0166-1280. DOI: https://doi.org/10.1016/j.theochem.2004.02.042. URL: https://www.sciencedirect.com/science/article/pii/S0166128004001721.

[34] J B Williams et al. "Probing the dynamics of dissociation of methane following core ionization using three-dimensional molecular-frame photoelectron angular distributions." In: *Journal of Physics B: Atomic, Molecular and Optical Physics* 45.19 (Sept. 2012), p. 194003. DOI: 10.1088/0953-4075/45/19/194003. URL: https://dx.doi.org/10.1088/0953-4075/45/19/194003.

[35] M W Wong and L Radom. "Methane dication: planar but not square." In: *Journal of the American Chemical Society* 113.3 (Feb. 1989), p. 1155. DOI: 10.1021/ja00185a070. URL: https://doi.org/10.1021/ja00185a070.

[36] Ahmed H. Zewail. "Laser Femtochemistry." In: *Science* 242.4886 (1988), pp. 1645–1653. DOI: 10.1126/science.242.4886.1645. eprint: https://www.science.org/doi/pdf/10.1126/science.242.4886.1645. URL: https://www.science.org/doi/abs/10.1126/science.242.4886.1645.

[37] Y Zhang et al. "Dissociative ionization of N2 by fast electron impact: roles of molecular orbitals." In: *Journal of Physics B: Atomic, Molecular and Optical Physics* 50.20 (Sept. 2017), p. 205202. DOI: 10.1088/1361-6455/aa8b51. URL: https://dx.doi.org/10.1088/1361-6455/aa8b51.

Erklärung

Ich versichere, dass ich diese Arbeit selbstständig verfasst und keine anderen als die angegebenen Quellen und Hilfsmittel benutzt habe.

Heidelberg, den 28.08.2023,